Exotic topological phonon modes in semiconductors: Symmetry analysis and first-principles calculations for representative examples

Guangqian Ding,[1,*] Chengwu Xie,[2,3,*] Jialin Gong,[2,*] Jianhua Wang,[2] Jingbo Bai,[2] Wenhong Wang,[3] Dengfeng Li,[1] Xiao-Ping Li,[4,†] and Xiaotian Wang[2,5,‡]

[1]*School of Science, Chongqing University of Posts and Telecommunications, Chongqing 400065, China*
[2]*School of Physical Science and Technology, Southwest University, Chongqing 400715, China*
[3]*School of Electronics & Information Engineering, Tiangong University, Tianjin 300387, China*
[4]*School of Physical Science and Technology, Inner Mongolia University, Hohhot 010021, China*
[5]*Institute for Superconducting and Electronic Materials (ISEM), University of Wollongong, Wollongong 2500, Australia*

(Received 29 April 2023; revised 8 July 2023; accepted 31 July 2023; published 10 August 2023)

Nowadays, it is recognized that semiconductors are prospective candidates for promising thermoelectric materials and the gapless topological phonon modes can result in a high phonon scattering rate. Therefore it is necessary to identify the topological phonons in semiconductors, which will aid future research aimed at gaining a better understanding of the thermoelectric properties of semiconductors. Using first-principles calculations and symmetry analysis, we propose a series of semiconductors as excellent candidates for the presence of exotic topological phonons. Remarkably, almost all the types of topological phonons, including various cases of Weyl/Dirac/triple point phonons, sextuple point phonons, nodal line phonons with different shapes and degenerates, and one-, two-, and three-nodal surface phonons can be observed in the phonon curves of these proposed semiconductors, revealing the ubiquitous existence of topological phonon modes in semiconductors. Moreover, the diverse types of topological phonons induce rich types of phononic surface modes in the surface orientations of semiconductors, which is advantageous to surface physics research.

DOI: 10.1103/PhysRevB.108.075201

I. INTRODUCTION

The discovery of the quantum spin Hall effect [1–4] and topological insulators [5–10] more than a decade ago transformed current condensed matter physics. Topological states of matter are currently one of the most active and fruitful research fields for experimentalists and theorists. A topological insulator is a unique type of topological material in which a band inversion occurs compared to an atomic insulator, resulting in a gapless surface state. Following that, topological states in metallic/semimetallic systems [11–19] were anticipated, and numerous topological metal/semimetal phases, such as nodal-point [20–24], nodal-line [25–29], and nodal-surface [30–34] phases, were harvested in a variety of materials. Topological semimetals/metals have unusual electronic structures that lead to protected surface states and a novel response to external fields, attracting intense study interest. Because of their excellent tunability and compatibility with the modern electronic industry, semiconductor materials [35–39] are particularly useful for devices compared to metal and semimetal materials. Hence, incorporating topological states into semiconductors may present new opportunities for designing future semiconductor electronic and optoelectronic devices. In 2019, Ideue *et al.* [40] extended the investigations of Weyl particles from the semimetals/metals to semiconductors. They [40] showed that the elemental semiconductor tellurium is a Weyl semiconductor with characteristic Weyl signatures, such as negative longitudinal magnetoresistance, planar Hall effect, and fascinating logarithmically periodic magneto-oscillations in the quantum limit regime. The predictions of Weyl fermions in semiconductors [40,41] provide a straightforward platform for investigating novel Weyl physics and topological device applications based on semiconductors, as well as confirming the universality of discrete scale invariance in topological materials. In 2022, Fu *et al.* [42] generalized the Dirac particles from semimetal to semiconductor in two dimensions (2Ds). Note that the 2D materials [43] have advantageous mechanical qualities and a compact size for integration and regulation.

In 2010, Zhang *et al.* [44] linked the phonon Hall conductivity with the Berry curvature of the phonon spectrum, revealed the topological signatures of phonons, and discovered a phase transition in the phonon Hall effect. It is worth noting that advances in Berry-phase physics and topological physics have resulted in the emergence of topological phononics [45–55]. Several researchers have recently studied topological quasiparticles in phonons, which describe the atomic lattice vibrations in solids. Contrary to the electronic bands, all the phonon branches are relevant for experimental detection, as the Pauli exclusion principle and Fermi surface constraints do not govern the phonons. Topological phonons [45–49,56–60] may also lead to novel phenomena related to heat transfer, phonon scattering, and electron-phonon

*These authors contributed equally to this work.
†Corresponding author: xpli@imu.edu.cn
‡Corresponding author: xiaotianwang@swu.edu.cn

TABLE I. Representative examples of 3D and 2D semiconductors with exotic topological phonon modes.

Topological phonon modes	Semiconductor	Section
3D		II-XI
WP phonons		II-VI
C-1 WP phonons	Ag_2HgI_4 (SG No. 111)	II
C-2 WP phonons	$SrGeTeO_6$ (SG No. 149), HgO (SG No. 152)	III, IV
C-3 WP phonons	Y_3CuGeS_7 (SG No. 173)	V
C-4 WP phonons	SbIrS (SG No. 198)	VI
DP phonons	SbIrS (SG No. 29), Ge_3N_4 (SG No. 176), TeO_2 (SG No. 19), $Ge_{19}(PBr)_4$ (SG No. 218)	VII
TP phonons	$MgTe_2$ (SG No. 205),ZrSO (SG No. 198), MgTe (SG No. 186), Hf_3N_4 (SG No. 220)	VIII
SP phonons	Hf_3N_4 (SG No. 220)	IX
NL phonons		X
WNL and DNL phonons	$RbGaH_2$ (SG No. 62)	X.1
Open and close WNL phonons	CsNaSe (SG No. 129)	X.2
NL phonons with different shapes	CdS_2 (SG No. 205), Au_2S (SG No. 224), Tl_2PtCl_6 (SG No. 225) K_2S (SG No. 225), LiBeN (SG No. 14)	X.3
NS phonons	AgI (SG No. 186), $YAgTe_2$ (SG No. 113), CdO_2 (SG No. 205)	XI
2D		XII
VWP and QNP phonons	$PtSe_2$ (LG No. 72)	XII
DP phonons	PbO (LG No. 45)	XII

interactions. For example, topological phonons can enhance the thermoelectric properties of materials [56]. The thermoelectric performance of a material is represented by the dimensionless figure of merit as follow:

$$zT = \frac{S^2\sigma T}{\kappa_e + \kappa_l}, \tag{1}$$

where S is the Seebeck coefficient, σ is the electrical conductivity, and κ_e and κ_l are the electronic and phononic contributions to thermal conductivity, respectively. It is known that high thermoelectric performance requires high electronic transport performance ($S^2\sigma$) while low thermal conductivity ($\kappa_e + \kappa_l$). Singh *et al.* [56] proposed that the gapless topological phonon modes in topological phononic materials can provide additional scattering channels in the three phonon-phonon scattering processes to decrease the mean free path and suppress κ_l. More importantly, compared to metals, narrow-gap semiconductors have much higher thermoelectric performance, which can be attributed to the following reasons: (1) a moderate carrier concentration in narrow-gap semiconductors contributes to the excellent electronic performance, i.e., the power factor $S^2\sigma$. (2) the κ_e is lower than metal due to its smaller level of charge carriers. Nowadays, it is recognized that semiconductors are prospective candidates for promising thermoelectric materials, which can be used in thermoelectric devices.

Therefore it is necessary to identify the topological phonons in semiconductors, which will aid future research aimed at obtaining a better understanding of the thermoelectric properties of semiconductors. In this work, we focused on the topological phonons and related phononic surface states in a series of realistic semiconductors. We show that almost all types of topological phonons can be observed in the phonon curves of the studied semiconductors, revealing the ubiquitous existence of topological phonon modes in semiconductors. We will analyze the symmetry of the space groups (SGs) and layer groups (LGs) for chosen 3D and 2D candidate semiconductors to gain a deeper understanding of the occurrence of topological phonons in these semiconductor materials. Moreover, we will discuss the nontrivial phonon surface/edge states related to these topological phonon bulk modes in semiconductors.

Generally, topological phonons in 3D can be divided based on the dimension of degeneracy manifold. For the dimension of the degeneracy manifold, we term the 0D, 1D, and 2D band degeneracy as point, line, and surface, respectively. In Secs. II–IX, we will exhibit the nodal point phonons in a series of 3D realistic semiconductors (see Table I for details). The nodal point phonons can be classified based on the degree of degeneracy. We term the two-, three-, four-, and six-degeneracy point phonons as Weyl, triple, Dirac, and sextuple point phonons, respectively. The discussion about the Weyl point (WP) phonons, Dirac point (DP) phonons, triple point (TP) phonons, and the sextuple point (SP) phonons in 3D realistic semiconductors can be found in Secs. II–VI, VII, VIII, and IX, respectively. Moreover, according to the topological charge $\mathcal{C}$ that equals ±1, ±2, ±3, and ±4, the WPs in Secs. II–VI can be divided into charge-one (C-1) WPs, C-2 WP, C-3 WPs, and C-4 WPs, respectively. The results concerning the C-1, C-2, C-3, and C-4 WPs phonons in realistic 3D semiconductors are presented in Secs. II, III–IV, V, and VI, respectively.

For the classification of nodal line (NL) phonons, the degree of degeneracy for the nodal lines (refer to Sec. X 1), whether the nodal lines traverse the BZ (refer to Sec. X 2), and the connection patterns of band crossings for the nodal lines (refer to Sec. X 3) are taken into account. Notably, in Sec. X 3, the nodal line phonons with different geometric shapes, including nodal link phonons, DNL net phonons, WNL net phonons, nodal box phonons, nodal chain phonons, and nodal cage phonons, in realistic 3D semiconductors are presented.

For the nodal surface (NS) phonons, they can be divided into three classes: one-NS, two-NS, and three-NS phonons

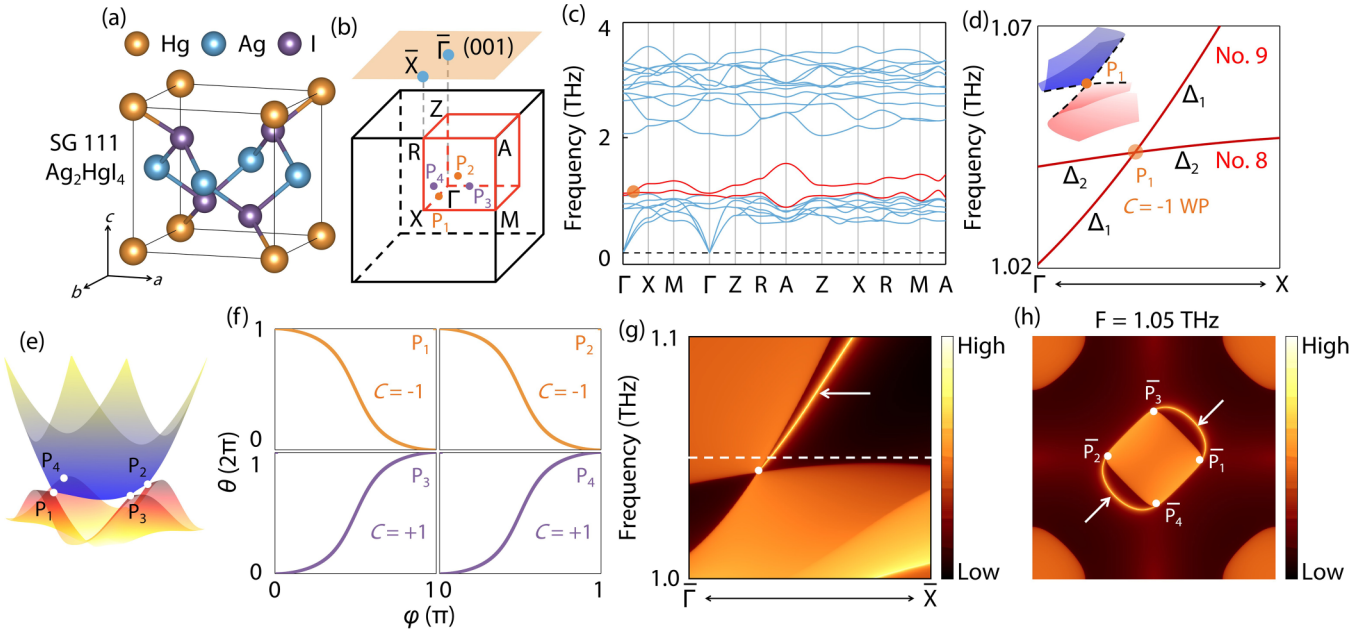

FIG. 1. (a) Crystal structure for P$\bar{4}$2m type Ag_2HgI_4. (b) 3D bulk and 2D surface BZs, and the positions of the minimum of four C-1 WPs in the 3D BZ. (c) Phonon dispersion for Ag_2HgI_4 along the $\Gamma - X - M - \Gamma - Z - R - A - Z - X - R - M - A$ high-symmetry paths. (d) Enlarged phonon bands on the $\Gamma - X$ path and the (co)representations for the two phonon bands. A P1 WP with type-II dispersion is obvious. (e) 3D plot of the minimum of four C-1 WPs in the $k_x - k_y$ plane. (f) The evolution of the average position of Wannier centers for P1 and P2 WPs with negative chirality or P3 and P4 WPs with positive chirality. (g) The calculated phonon local density of states (LDOS) of Ag_2HgI_4. (h) The constant frequency slice at 1.05 THz projected on the semi-infinite (001) surface.

host one, two, and three pair(s) of NS states on one, two, and three the $k_i = \pm\pi$ ($i = x$, y, and z) planes, respectively. The results concerning the one-NS, two-NS, and three-NS phonons in realistic 3D semiconductors are presented in Sec. XI.

To this date, research into gapless topological phonon states in 2D materials is very limited. In Sec. XII, two 2D experimentally feasible semiconductors, $PtSe_2$ and PdO, were also reported to host rich topological phonons, including valley Weyl point (VWP) phonons, quadratic nodal point (QNP) phonons, and Dirac phonons (see Table I for details).

II. A MINIMUM OF C-1 WP PHONONS IN SEMICONDUCTOR Ag_2HgI_4

C-1 WP, also named conventional WP, is a zero-dimensional (0D) twofold band degeneracy. C-1 WP enjoys relativistic linear dispersion along any direction in momentum space and can appear in 3D crystals without any space group symmetry (except translation symmetry). In 2019, Xia *et al.* [61] proposed that CdTe with the space group (SG) 216–a well-known synthesized II-VI semiconductor–to exhibit 12 C-1 WPs in its phonon curves. It is highly desirable to investigate synthesized semiconductors containing minimum C-1 Weyl phonons to show the topological features of C-1 Weyl phonons intuitively. It was widely believed that nonmagnetic systems should have a minimum of four C-1 WPs. The following is the argument. Assume a C-1 WP with charge $\mathcal{C} = 1$ is located at k in the BZ. If the time-reversal symmetry $\mathcal{T}$ is preserved, another C-1 WP with the same charge $\mathcal{C} = 1$ must exist at k. Due to the no-go theorem, at least two additional C-1 WPs at $-k$ (each with charge $\mathcal{C} = -1$) are necessary to guarantee the chiral charge neutrality of the BZ.

This Sec. focuses on the semiconductor Ag_2HgI_4 [62], one of the oldest known compounds that showed thermochromic behavior, and demonstrates that its phonon curves contain a minimum of four C-1 WPs. Ag_2HgI_4 has garnered significant interest as a potential recording medium material, particularly in the infrared region, as well as a promising superionic conductor, which is vital in solid-state batteries and prospective optical devices. The phonon dispersion curves for P$\bar{4}$2m-type Ag_2HgI_4 along the high-symmetry paths are shown in Fig. 1(c).

We focus on the numbers (Nos.) 8 and 9 phonon branches around the frequency of 1.04 THz in the phonon curves [see Fig. 1(c)]. From it, one finds that the two phonon branches only cross with each other along the $\Gamma - X$ path, forming a twofold degenerate point labeled as P1 [see Fig. 1(d)]. We investigated the topological feature of the band crossing P1 by evaluating the average Wannier charge center (WCC) over a sphere enclosing the crossing point. One can see the winding number of WCC is -1 for the degenerate point P1 along the $\Gamma - X$ path, respectively. This indicates that the twofold degenerate P1 point is a WP with $\mathcal{C} = -1$. Considering the crystal symmetry and $\mathcal{T}$, there are a total of four such WPs in the 3D BZ [see Fig. 1(e)], and the positions of the minimum of four C-1 WPs with opposite $\mathcal{C}$ (two WPs with $\mathcal{C} = 1$, and other two WPs with $\mathcal{C} = -1$) in Ag_2HgI_4 are exhibited in Figs. 1(e) and 1(f). Moreover, the WPs in Ag_2HgI_4 have a tilted cone dispersion and belong to type-II WPs [63–65], as shown in Fig. 1(d).

The appearance of the WP on the $\Gamma - X$ path can be understood from the symmetry analysis as follows: The little co-group of $\Gamma - X$ path is C_2, and the crossing bands can be labeled by two distinct 1D irreducible representations (IRRs), Δ_1 and Δ_2 [see Fig. 1(d)], and the corresponding eigenvalues of C_{2y} are ± 1. It implies that a C-1 WP can appear once band inversion occurs, as shown in Fig. 1(d). We construct a $k \cdot p$ effective model based on symmetry analysis to characterize this WP. The basis is chosen as eigenstates of C_{2y} with $|+1\rangle$ and $|-1\rangle$, and the matrix representations of the generators can be expressed as $C_{2y} = \sigma_z$ and $C_{2z}\mathcal{T} = \sigma_0$. The effective Hamiltonian retained to the leading order reads

$$\mathcal{H}^{111}_{\Gamma\text{-}X} = (c_1 + c_2 k_y)\sigma_0 + c_3 k_y \sigma_z + c_4 k_x \sigma_x + c_5 k_z \sigma_y, \qquad (2)$$

where c_i are real parameters, $\sigma_{i=x,y,z}$ are the Pauli matrices, and σ_0 is the 2×2 identity matrix. It is worth noting that $c_2 k_y \sigma_0$ is a linear tilt term, and when $|c_2/c_3| > 1$, the Hamiltonian $\mathcal{H}^{111}_{\Gamma\text{-}X}$ describes a type-II WP.

Although the C-1 WPs can be identified by symmetry analysis, the type of band dispersion around the WPs cannot be directly determined by symmetry analysis. Hence, the quest for C-1 WP materials with ideal type-II WPs continues to be a challenge.

The calculated phonon local density of states (LDOS) and surface arcs for the semi-infinite (001) surface of Ag_2HgI_4 are exhibited in Figs. 1(g) and 1(h), respectively. From Fig. 1(h), one finds that two arcs, connecting the projections of the two C-1 WPs with opposite $\mathcal{C}$, are apparent on the semi-infinite (001) surface. According to Fang *et al.* [66], the phononic arc surface states of a C-1 WP around the projected point on the boundary correspond to a helicoid.

III. A MINIMUM OF C-2 WP (C-2 SINGLE-PAIR-WEYL-POINT) PHONONS IN SEMICONDUCTOR $SrGeTeO_6$

Fang *et al.* [67] demonstrated in 2012 that, with rotation symmetry, two (three) conventional WPs could combine to form an unconventional WP with higher topological charge $|\mathcal{C}| = 2$ ($|\mathcal{C}| = 3$) and quadratic (cubic) dispersion in the plane normal to the rotation axis. Recently, unconventional WP with a maximum $|\mathcal{C}|$ of 4, hosting a cubic dispersion along the [111] direction and quadratic dispersion in all other directions, has been proposed in spinless and spinful systems [68–70].

According to our previous work [71], the $|\mathcal{C}|$ of a WP located at a time-reversal-invariant momentum point must be even (i.e., 2 and 4) in a spinless system. More interestingly, we pointed out that only two C-2 WPs or C-4 WPs could exist at two time-reversal-invariant momenta. Hence, the two C-2 WPs or C-4 WPs located at the two time-reversal-invariant momenta points can be named single-pair-Weyl-points in spinless systems.

Generally, it would be better to realize Weyl systems with as few WPs as possible to have a clean platform to investigate the properties of WPs. Keeping the number of WPs to a minimum will simplify both the theoretical model and the transport experiments [72,73]. In addition, the surface states created by the smallest number of WPs are easily observed in spectroscopy investigations.

In this section, we shall select the P312 $SrGeTeO_6$ semiconductor [74] as an example to show the C-2 single-pair-Weyl-point phonons in its phonon curves. The phonon dispersion for P312 $SrGeTeO_6$ is exhibited in Fig. 2(c). The enlarged phonon curves in the frequency region of 14.6–15.0 THz are shown in Fig. 2(d). From it, one finds the Nos. 18 and 19 phonon branches can only form two crossing points at the Γ and A time-reversal-invariant momenta points in the 3D BZ [see the insert figure of Fig. 2(d)]. As shown in Fig. 2(e), these two crossing points at the Γ and A are C-2 WPs with $|\mathcal{C}| = 2$.

In Figs. 2(f) and 2(g), we exhibit the projected spectrum on the semi-infinite (010) surface and the constant frequency slice at 14.7 THz of $SrGeTeO_6$. From Fig. 2(g), one finds that the surface modes of the single-pair-Weyl-point phonons could form a closed noncontractible loop that winds around the surface BZ along only one direction. This type of surface mode is distinct from the open arcs of the C-1 WP phonons.

Note that multi-charged WPs are stabilized by crystalline symmetry in single-pair-Weyl-point states. The appearance of the C-2 WPs at the Γ and A in SG 149 arises from the essential band degeneracy; both of them are protected by 2D IRR E of D_3 little cogroup and thus have the same form of effective Hamiltonian. Under the basis of IRR E, the matrix representation of generators of D_3 group can be expressed as, $C_3^+ = \cos\frac{2\pi}{3}\sigma_0 - \mathrm{i}\sin\frac{2\pi}{3}\sigma_y$, $C'_{21} = \sigma_z$, and antiunitary operation $\mathcal{T} = -\sigma_0$.

The effective Hamiltonian around the Γ and A in SG 149, to the leading order, takes the following form:

$$\mathcal{H}^{149}_{\Gamma,\mathrm{A}} = c_1\left(k_x^2 + k_y^2\right)\sigma_0 + (c_2 k_x k_y + c_3 k_x k_z)\sigma_x + \left[c_4\left(k_x^2 - k_y^2\right) + c_5 k_y k_z\right]\sigma_z + c_6 k_z \sigma_y. \qquad (3)$$

One can observe that Hamiltonian $\mathcal{H}^{149}_{\Gamma,\mathrm{A}}$ exhibits linear band dispersion along the k_z direction and quadratic dispersion for the $k_x - k_y$ plane, which describes a C-2 WP.

Under perturbations that reduce symmetry, they should typically split into several WPs with unit charge. In consequence, the closed surface loop will split into open arcs [71].

IV. TYPE-III C-2 WP-BASED WEYL COMPLEX PHONONS IN SEMICONDUCTOR HgO

According to the Nielsen-Ninomiya no-go theorem [75,76], there is always an equal number of WPs with opposing chirality (see the cases in Secs. II and III); hence the total topological charge is always zero. However, the emergence of WPs in pairs is not necessary for the conservation of chiral charge if a system simultaneously possesses WPs with distinct $|\mathcal{C}|$. Wang *et al.* [77] and Huang *et al.*, [78], for instance, presented a symmetry-protected three-terminal Weyl complex whose phonon branches can form a C-2 WP and two C-1 WPs (for a total of three WPs) in realistic materials with trigonal, hexagonal, and cubic lattices.

In this section, the well-known chiral binary compound HgO [79] with the chiral space group 152 and a semiconducting band structure was chosen to demonstrate that it can host a C-2 WP with type-III dispersion [80,81] and two C-1 WPs, generating a three-terminal Weyl complex in its phonon curves. The phonon dispersion for $P3_121$-type HgO is shown in Fig. 3(c), and we focus on the Nos. 14 and 15 phonon

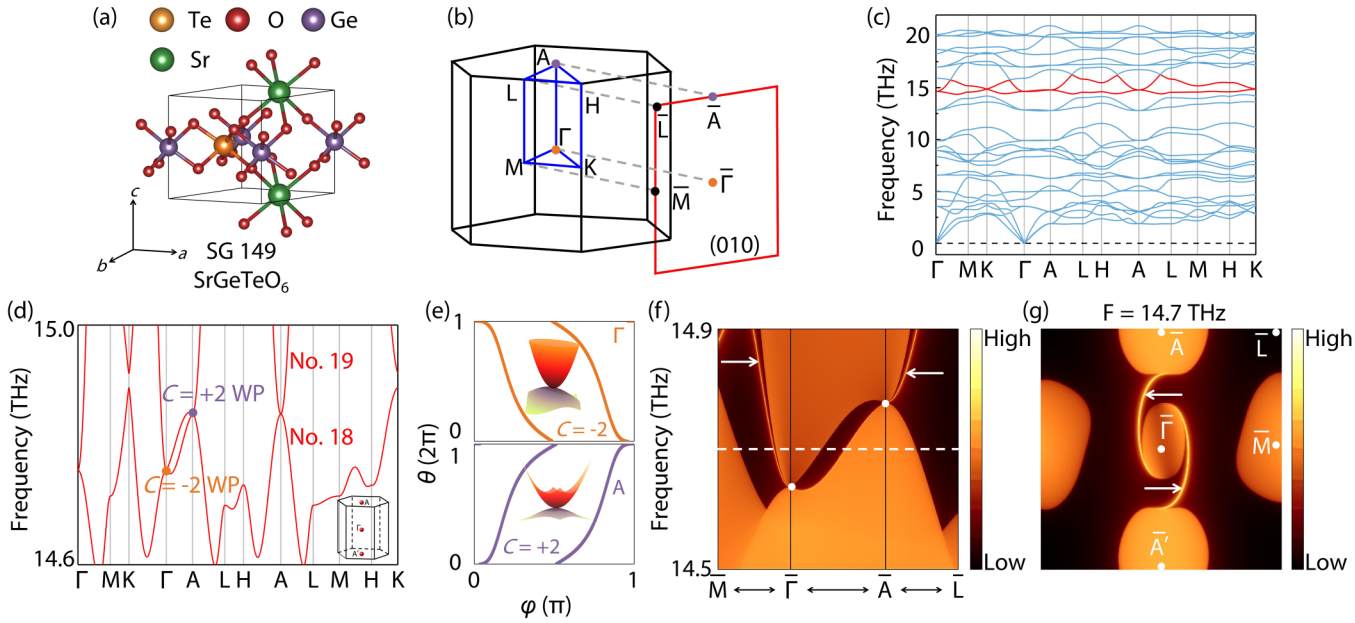

FIG. 2. (a) Crystal structure for P312 type $SrGeTeO_6$. (b) 3D bulk and 2D surface BZs. (c) Phonon dispersion for $SrGeTeO_6$ along the $\Gamma - M - K - \Gamma - A - L - H - A - L - M - H - K$ high-symmetry paths. (d) Enlarged phonon bands and the positions of the minimum of two C-2 WPs in the 3D BZ. (e) The evolution of the average position of Wannier centers for two C-2 WPs at the Γ and A points with negative and positive chirality. Inserts are the 3D plot of the two C-2 WPs in the $k_x - k_y$ plane. (f) The calculated phonon LDOS of $SrGeTeO_6$. (g) The constant frequency slice at 14.7 THz projected on the semi-infinite (010) surface.

branches around the frequency of 13 THz. Figure 3(c) shows that the two phonon branches form a crossing point at the Γ point and a crossing point at the K point. Actually, the crossing point at the Γ belongs to a C-2 WP with $\mathcal{C} = -2$, and the crossing point at the K belongs to a C-1 WP with $\mathcal{C} = 1$ [see Fig. 3(d)], respectively. We would like to point out that the proposed C-2 WPs in phonon systems by Wang *et al.* [77] and Huang *et al.* [78] have a type-I phonon band dispersion. However, the C-2 WP in $P3_121$-type HgO has a type-III phonon band dispersion, that is, the phonon band dispersion around the C-2 WP in the $k_x - k_z$ plane shows a saddle shape [see Fig. 3(d)], and there are two connected

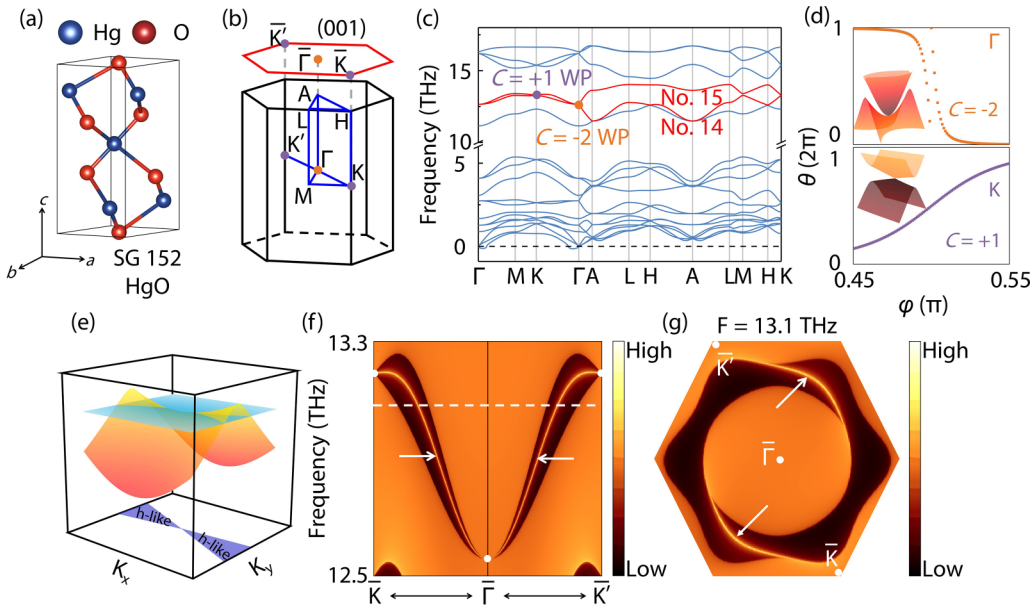

FIG. 3. (a) Crystal structure for $P3_121$-type HgO. (b) 3D bulk and 2D surface BZs. (c) Phonon dispersion for HgO along the $\Gamma - M - K - \Gamma - A - L - H - A - L - M - H - K$ high-symmetry paths. (d) The evolution of the average position of Wannier centers for a C-2 WP at the Γ point with negative chirality and a C-1 WP at the K point with positive chirality. Inserts are the 3D plot of the C-2 WP and C-1 WPs in the $k_y - k_z$ and $k_x - k_y$ planes, respectively. (e) Constant-frequency surface (highlighted by blue surface) of the type-III C-2 WP at the Γ point contains two connected h-like states. (f) The calculated phonon LDOS of HgO. (g) The constant frequency slice at 13.1 THz projected on the semi-infinite (001) surface.

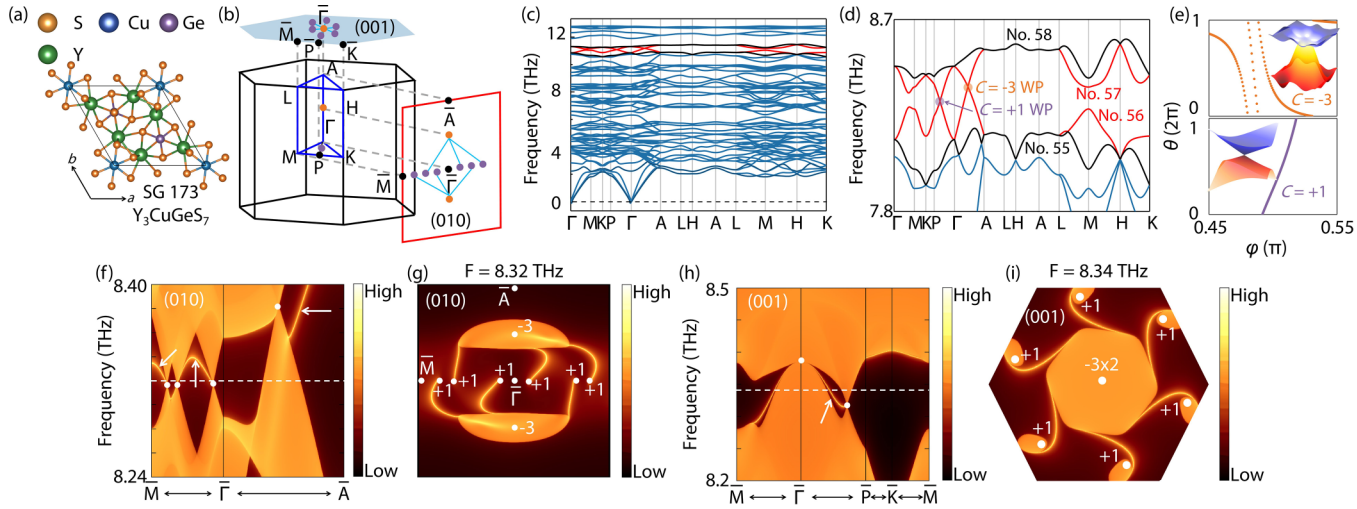

FIG. 4. (a) Crystal structure for P6$_3$-type Y_3CuGeS_7. (b) 3D bulk and 2D surface BZs. The schematics of the triple-helicoid and the sextuple-helicoid surface modes on (010) and (001) surfaces, respectively. (c) Phonon dispersion for Y_3CuGeS_7 along the $\Gamma - M - K - P - \Gamma - A - L - H - A - L - M - H - K$ high-symmetry paths. (d) The enlarged phonon curves, including No. 55–58 phonon branches, in the frequency region of 7.8–8.7 THz. (e) The evolution of the average position of Wannier centers for a C-3 WP on the $\Gamma - A$ path with negative chirality and a C-1 WP on the P-Γ with positive chirality. Inserts are the 3D plot of the C-3 WP and C-1 WPs in the $k_x - k_y$ plane. [(f) and (h)] The calculated phonon LDOS of Y_3CuGeS_7 on the semi-infinite (010) and (001) surfaces, respectively. (g) The constant frequency slice at 8.32 THz projected on the semi-infinite (010) surface. (i) The constant frequency slice at 8.34 THz projected on the semi-infinite (001) surface.

holelike (h-like) states in the constant-frequency surface at the C-2 WP at the Γ point [see Fig. 3(e)].

The same C-1 WP with $\mathcal{C} = 1$ can also be found at the K' point, and therefore, the one type-III C-2 WP at the Γ point (with $\mathcal{C} = -2$) and two C-1 WPs at the K and K' points (each with $\mathcal{C} = 1$) will form a Weyl complex, for which the net topological charge vanishes. In contrast to traditional Weyl systems with pairs of C-1 WPs, in which surface arcs terminate at the projections of two C-1 WPs with opposing chirality [see Fig. 1(h)], the phonon surface arcs of the Weyl complex in HgO connect the projections of one C-2 WP and two C-1 WPs [see Fig. 3(g)]. Notably, the phononic surface arcs arising from the projections of the Weyl complex in P3$_1$21-type HgO are pretty long and span the entire (001) surface BZ. The majority of catalytic processes occur on surfaces. Meng *et al.* [82] recently established a linear relationship between catalytic enhancement and surface arc length. Consequently, the extremely long phononic surface arcs on the (001) surface may facilitate catalysis if the phonon frequency is in resonance with certain midsteps in the reaction [83].

Before closing this section, we would like to explain the appearance of the type-III Weyl complex in $P3_121$-type HgO from the symmetry viewpoint: similar to the symmetry protection of the Γ point in space group $P312$, here, the type-III C-2 WP located at the Γ point in HgO is also derived from the 2D IRR of the D_3 group. Therefore the effective Hamiltonian of the Γ point in HgO shares the same form with $\mathcal{H}^{149}_{\Gamma,A}$, reads

$$\mathcal{H}^{152}_{\Gamma} = c_1\left(k_x^2 + k_y^2\right)\sigma_0 + (c_2 k_x k_y + c_3 k_x k_z)\sigma_x + \left[c_4\left(k_x^2 - k_y^2\right) + c_5 k_y k_z\right]\sigma_z + c_6 k_z \sigma_y. \quad (4)$$

Here, the tilt term $c_1(k_x^2 + k_y^2)\sigma_0$ determines the type of WPs, and when $|c_1/c_4| > 1$, the Hamiltonian $\mathcal{H}^{152}_{\Gamma}$ describes a type-III C-2 WP. In addition, there are two other C-1 WPs in HgO, which are located at the K and K' points, respectively, and carry the same chirality related by $\mathcal{T}$. The effective Hamiltonian around the K and K' can be described by

$$\mathcal{H}^{152}_{K} = c_1(k_x\sigma_x + k_y\sigma_z) + c_2 k_z \sigma_y. \quad (5)$$

The C-2 WPs at the Γ and C-1 WPs at the $K(K')$ point form a unique Weyl complex.

V. C-3 WPS-BASED WEYL COMPLEX PHONONS IN SEMICONDUCTOR Y_3CuGeS_7

Besides the semiconductor with C-2 WP-based Weyl complex phonons mentioned in Sec. IV, we shall note that the semiconductor Y_3CuGeS_7 [84] can host C-3 WPs-based Weyl complex phonons and attractive phononic surface states. The phonon dispersion for Y_3CuGeS_7 along the $\Gamma - M - K - M_1 - \Gamma - A - L - H - A|L - M|H - K$ paths is shown in Fig. 4(c), and we focus on the enlarged phonon curves in the frequency region of 7.8–8.7 THz [see Fig. 4(d)]. At a first glance, one finds that the No. 56 and No. 57 phonon branches can form two crossing points, one along the $\Gamma - A$ path and the other along the $P - \Gamma$ path. These two points belong to C-3 WP with $\mathcal{C} = -3$ and C-1 WP with $\mathcal{C} = 1$, respectively, as shown in Fig. 4(e). Totally, there should be two C-3 WPs and six C-1 WPs, forming a Weyl complex, in the 3D BZ.

Note that the C-3 WP in Y_3CuGeS_7 is the neck crossing point of the hourglass-like shape [85–88], composed of four phonon branches with Nos. 55–58, on the $\Gamma - A$ path. Notably, the hourglass quasiparticle [85–88] has garnered much attention, as the neck crossing point of an hourglass-type band represents a new kind of essential degeneracy that cannot be inferred directly from the IRRs of the corresponding little group.

Here, we mainly focus on the neck of the hourglass bands, i.e., the band crossing point formed by the phonon branches Nos. 56 and 57. Two distinct 1D IRRs can label these two bands Δ_3 and Δ_6 of C_6 group, and the corresponding eigenvalues of $\widetilde{C}_{6z} = \{C_{6z} \mid 00\frac{1}{2}\}$ are $e^{\frac{i\pi}{3}}$ and $e^{-\frac{2i\pi}{3}}$. Under the basis of $|e^{\frac{i\pi}{3}}\rangle \oplus |e^{-\frac{2\pi i}{3}}\rangle$, the matrix representation of $\widetilde{C}_{6z}$ is given by $\widetilde{C}_{6z} = e^{\frac{i\pi}{3}}\sigma_z$. As a consequence, the effective model at the $\Gamma - A$ path of Y_3CuGeS_7 could be written in the form of

$$\mathcal{H}^{173}_{\Gamma\text{-}A} = H_0 + \left[(\alpha_1 k_+^3 + \alpha_2 k_-^3)\sigma_+ + \text{H.c.}\right]. \tag{6}$$

With

$$H_0 = \sum_{i=0,x,y,z} \sigma_i\left[c_{i,1}k^2 + c_{i,2}k_z^2 + c_{i,3}k_z\left(1 + c_{i,4}k^2 + c_{i,5}k_z^2\right)\right], \tag{7}$$

where $c_{i,j}$ are real parameters, $k^2 = k_x^2 + k_y^2 + k_z^2$, $k_\pm = k_x \pm ik_y$, and $\sigma_\pm = \sigma_x \pm i\sigma_x$. The Hamiltonian $\mathcal{H}^{173}_{\Gamma-A}$ exhibits linear band splitting along the k_z direction and cubic band splitting in k_x-k_y plane, which indicates the presence of the C-3 Weyl point.

Next, we come to show the appearance of triple- and sextuple-helicoid surface arc states related to the Weyl complex formed by two hourglass C-3 WPs and six C-1 WPs. If we consider the semi-infinite (010) surface, the two hourglass C-3 WPs with $\mathcal{C} = -3$ and six C-1 WPs with $\mathcal{C} = 1$ will be projected to different positions on the (010) surface, and each C-3 WP combines three C-1 WPs forming three surface arcs, i.e., a triple-helicoid surface state [see Fig. 4(g)]. However, if we consider the semi-infinite (001) surface, the six C-1 WPs with $\mathcal{C} = 1$ will be projected to different positions, and the two hourglass C-3 WPs will be projected to the same position. Thus six surface arcs connected to the $\bar{\Gamma}$ point, forming a sextuple-helicoid surface state [as shown in Fig. 4(i)] because $\mathcal{C} = -3\times 2$.

VI. A SINGULAR C-4 WP SURROUNDED BY CHARGED NODAL WALLS IN SEMICONDUCTOR SbIrS

Weyl particles in any crystal are widely assumed to be restricted by the so-called Nielsen-Ninomiya no-go theorem [75,76], which demands that WPs exist in pairs with opposing chirality. As shown in Fig. 1(d), surface arcs connecting the projections of the WPs on the surface BZ are a manifestation of WP pairs.

However, it is essential to understand that Weyl physics has only been discovered in the last decade, which is considerably later than the formulation of the no-go theorem proposed in 1981 [75,76], and therefore, this theorem does not provide a precise definition and derivation for its application to nodal walls. In 2020, Ma *et al.* [89] extended the original Nielsen-Ninomiya no-go theorem to account for the situation that topological nontrivial Weyl nodal walls surround a singular WP. Specifically, rather than searching for a pair of WPs with opposing chirality, the Berry curvature field of unpaired WPs can be absorbed by higher dimensional topological objects, such as 2D topological nontrivial Weyl nodal walls.

In this section, we would like to report that a singular C-4 WP surrounded by charged nodal walls appears in the phonon curves of the semiconductor SbIrS [90]. The phonon dispersion for SbIrS along the $\Gamma - X - M - \Gamma - R - X - R - M$ high-symmetry paths is exhibited in Fig. 5(d). From it, one finds that the No. 17 and No. 18 phonon branches degenerate with each other along the $R - X - R - M$ paths, reflecting the formation of the nodal walls on the $k_i = \pm\pi$ planes, which can be understood from the following symmetry analysis:

The lattice of SbIrS has the SG symmetry of $P213$ (No. 198), which contains three twofold screw rotations in SG 198. They are shown as $\widetilde{C}_{2x} = \{C_{2x} \mid \frac{1}{2}, \frac{1}{2}, 0\}$, $\widetilde{C}_{2y} = \{C_{2y} \mid 0, \frac{1}{2}, \frac{1}{2}\}$, and $\widetilde{C}_{2z} = \{C_{2z} \mid \frac{1}{2}, 0, \frac{1}{2}\}$. A combination of nonsymmorphic twofold screw-rotational symmetry and $\mathcal{T}$ can guarantee the nodal surfaces. We take $S_{2z}\mathcal{T}$ as an example, one can find that $(\widetilde{C}_{2z})^2 = T_{001} = e^{ik_z}$, $\mathcal{T}^2 = -1$. Thus the combination $\widetilde{C}_{2z}\mathcal{T}$ is an antiunitary operator, which satisfies $(\widetilde{C}_{2z}\mathcal{T})^2 = -1$ on the $k_z = \pm\pi$ plane and further lead to twofold Kramers degeneracy. This is the origin of the nodal surface on the $k_z = \pm\pi$ plane, and the same argument applies to the k_x and k_y planes. Hence, the nodal wall state appears.

Moreover, a crossing point, formed from the No. 17 and No. 18 phonon branches, can be found at the center of the 3D BZ, i.e., the Γ point. The crossing point at the Γ is a twofold degenerate Weyl point with $\mathcal{C} = -4$ [see Fig. 5(e)]. C-4 WP hosts a quadratic band dispersion along the k_x, k_y, and k_z directions and a cubic band dispersion along the [111] direction, which can be understood from the following symmetry analysis: The C-4 WP at the Γ in SG of $P213$ correspond to the 2D corepresentation $({}^1E^2E)$ of the T point group. Under the basis of ${}^1E^2E$, the symmetry generators are expressed as follows: $C_{31}^+ = \cos\frac{2\pi}{3}\sigma_0 + i\sin\frac{2\pi}{3}\sigma_z$, $C_{2z} = \sigma_0$, $C_{2y} = \sigma_0$, and $\mathcal{T} = \sigma_x$.

Under the symmetry constraints above, the effective Hamiltonian up to the third order is

$$\begin{aligned}\mathcal{H}^{198}_{\Gamma} &= c_1k^2\sigma_0 + c_2k_xk_yk_z\sigma_z + \sqrt{3}\left[c_3k_x^2 + c_4k_y^2 - (c_3 + c_4)k_z^2\right]\sigma_x \\ &\quad + \left[c_4\left(k_y^2 - 2k_x^2 + k_z^2\right) - c_3\left(k_x^2 - 2k_y^2 + k_z^2\right)\right]\sigma_y.\end{aligned} \tag{8}$$

The above effective Hamiltonian $\mathcal{H}^{198}_{\Gamma}$ describes a C-4 WP.

One can define the Chern number of the nodal surface using the Berry field theory, i.e., the Chern number of the nodal surface should be opposite to the net charge of all the WPs within one BZ, which results in a Chern number of zero for the BZ as a whole. The nonzero $\mathcal{C} = 4$ value for the Weyl nodal walls in SbIrS is caused by the absence of inversion symmetry. Hence, a singular C-4 WP and a topologically charged Weyl nodal surface with $\mathcal{C} = 4$ form a topologically charged Weyl point-surface system [91]. As shown in Figs. 5(f)–5(h), no arc surface state can be observed in the spectra, no matter how we change the number of slabs. The reason can be understood as follows: the C-1 Weyl pairs follow the no-go theorem and exhibit arc surface states, connecting the surface projection of the two WPs. The chiral edge modes for nontrivial 2D slices trace out the arc on the surface, as shown in Fig. 5(j). For the topologically charged Weyl point-surface system, the singular WP locates at the Γ point, surrounded by nodal walls covering the entire BZ boundary. The gapped 2D slices of the BZ, which are required for the topological argument of surface states, cannot be seen in Fig. 5(k); hence, the arc surface states vanish even though a WP exists in 3D BZ.

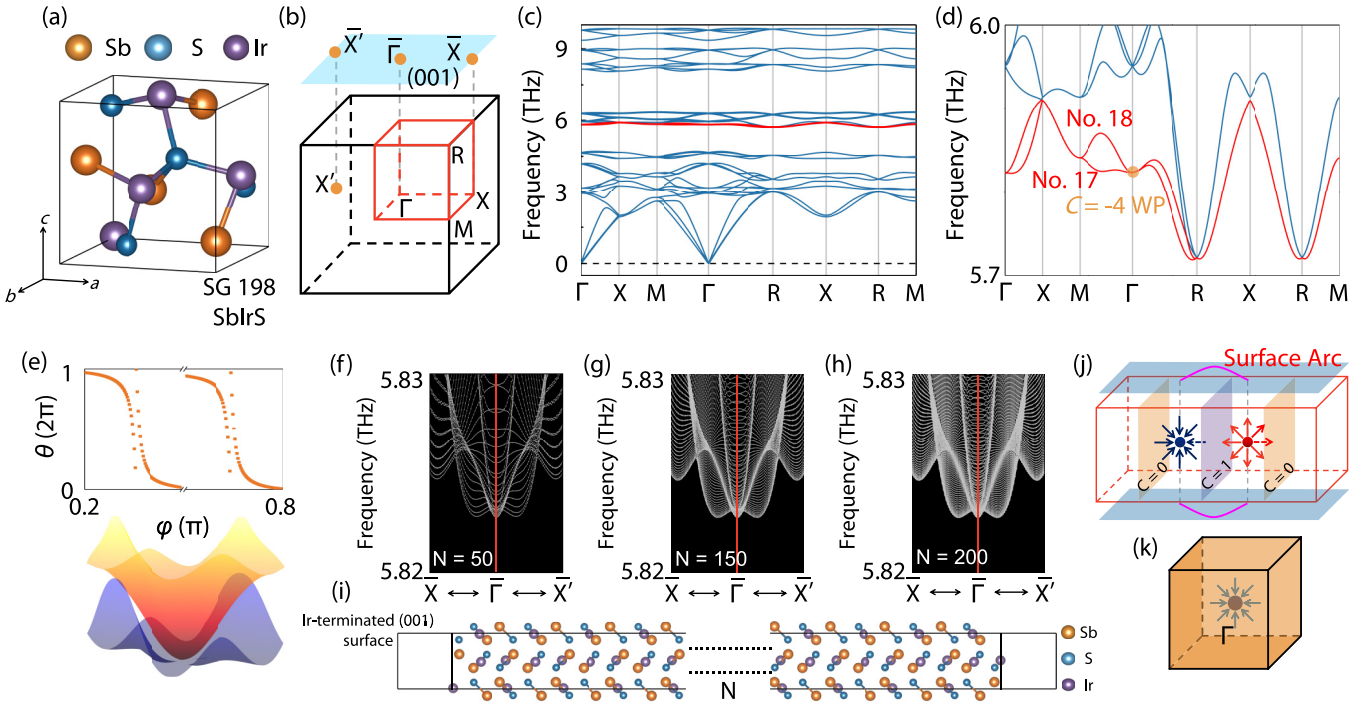

FIG. 5. (a) Crystal structure for $P213$-type SbIrS. (b) 3D bulk and 2D surface BZs. (c) Phonon dispersion for SbIrS along the $\Gamma - X - M - \Gamma - R - X - R - M$ high-symmetry paths. (d) The enlarged phonon curves, including No. 17 and No. 18 phonon branches in the 5.7–6.0 THz frequency region. (e) The evolution of the average position of Wannier centers for a C-4 WP at the Γ with negative chirality and the 3D plot of the C-4 WP in the $k_x - k_y$ plane. [(f)–(h)] Surface spectra on (001) surface calculated by a slab model. Different numbers (N) of slabs are considered during the calculations. (i) Ir-(001) surface terminations of SbIrS. (j) C-1 Weyl pairs respecting the no-go theorem and exhibiting arc surface states. (k) Topologically charged Weyl point-surface system and the disappearing arc surface states.

VII. DP, C-2 DP, QDP, AND CCDP PHONONS IN SEMICONDUCTORS

Fourfold degeneracy point phonons can be divided into four parts [70,92,93], DP, C-2 DP, QDP, and CCDP, respectively. We would like to point out that using first-principles computations, Zhang *et al.* [94] presented noncentrosymmetric material FeSi, a strongly correlated semiconductor, harboring C-2 DP phonons and C-2 TP phonons in its phonon dispersions. More importantly, the C-2 DP phonons and C-2 TP phonons were verified by Miao *et al.* [95] in parity-breaking FeSi with the help of inelastic x-ray scattering. In this section, we shall show the ubiquitous existence of phononic DP signatures in semiconductors.

For the DP, it is a 0D fourfold band degeneracy with a topological charge $\mathcal{C} = 0$. It features a linear dispersion along any direction in momentum space. This section shows that the SbIrS [90] semiconductor hosts DP phonons at the R point in the frequency around 10 THz [see Figs. 6(c) and 6(d)].

The $Pca2_1$ (No. 29) is a nonsymmorphic space group, which may lead to higher degeneracy at the boundary of the Brillouin zone. Indeed, the DP at the R corresponds to the 4D projective representation (R_1R_1). Under the basis of R_1R_1, the matrix representation of symmetry generators can be expressed as $C_{2z} = i\Gamma_{0,2}$, $M_y = i\Gamma_{0,1}$, and $\mathcal{T} = -\Gamma_{2,2}$. As a consequence, the effective Hamiltonian at the R point of SG 29 could be derived as

$$\mathcal{H}_R^{29} = c_1\Gamma_{0,0} + c_2\Gamma_{0,1}k_x + c_3\Gamma_{0,3}k_y + \sum_{i=1,2,3} c_{i,1}\Gamma_{i,0}k_z, \quad (9)$$

where $\Gamma_{i,j} = \sigma_i \otimes \sigma_j$ with $\sigma's$ referring to the Pauli matrix. The effective Hamiltonian $\mathcal{H}_R^{29}$ describes a linear DP.

For the QDP, it is a 0D fourfold band degeneracy with a topological charge $\mathcal{C} = 0$. It features a linear dispersion along the certain high-symmetry line, and has a quadratic band splitting in the plane normal to the high-symmetry line. We show that the semiconductor Ge_3N_4 [96] is a candidate material with a QDP at the A point in the frequency around 21.7 THz [see Fig. 6(g)]. Such a QDP hosts a linear dispersion along the $\Gamma - A$ path and a quadratic band splitting in the plane normal to the $\Gamma - A$ path [see Fig. 6(h)]. We then understand the physics of the QDP phonons in Ge_3N_4 via the following: The QDP at the A in $P6_3/m$ (No. 176) SG also corresponds to the 4D projective representation (A_1A_3). And the matrix representation of symmetry generators can be expressed as $C_6^+ = \sin(\frac{\pi}{3})\Gamma_{0,2} + i\cos(\frac{\pi}{3})\Gamma_{3,3}$, $\mathcal{I} = \Gamma_{0,1}$, and $\mathcal{T} = \Gamma_{1,0}$. As a consequence, the effective Hamiltonian at the A point of SG 176 could be derived as

$$\mathcal{H}_A^{176} = \left[c_1 + c_2\left(k_x^2 + k_y^2\right) + c_3k_z^2\right]\Gamma_{0,0} + c_4\Gamma_{3,3}k_z + (\alpha_1\Gamma_{+,1}k_-^2 + \alpha_2k_z\Gamma_{+,1}k_+ + \text{H.c.}). \quad (10)$$

Here, $\Gamma_{i,j} = \sigma_i \otimes \sigma_j$ and $\sigma_\pm = \frac{(\sigma_1 \pm i\sigma_2)}{2}$. α_i are complex parameters and $k_\pm = k_x \pm ik_y$. One can observe that the effective Hamiltonian $\mathcal{H}_A^{176}$ describes a QDP.

For the C-2 DP, it is a 0D fourfold band degeneracy with a topological charge $\mathcal{C} = \pm 2$. It features a linear dispersion along any direction in momentum space. We show that the semiconductor TeO_2 [97] is a candidate material with C-2 DP

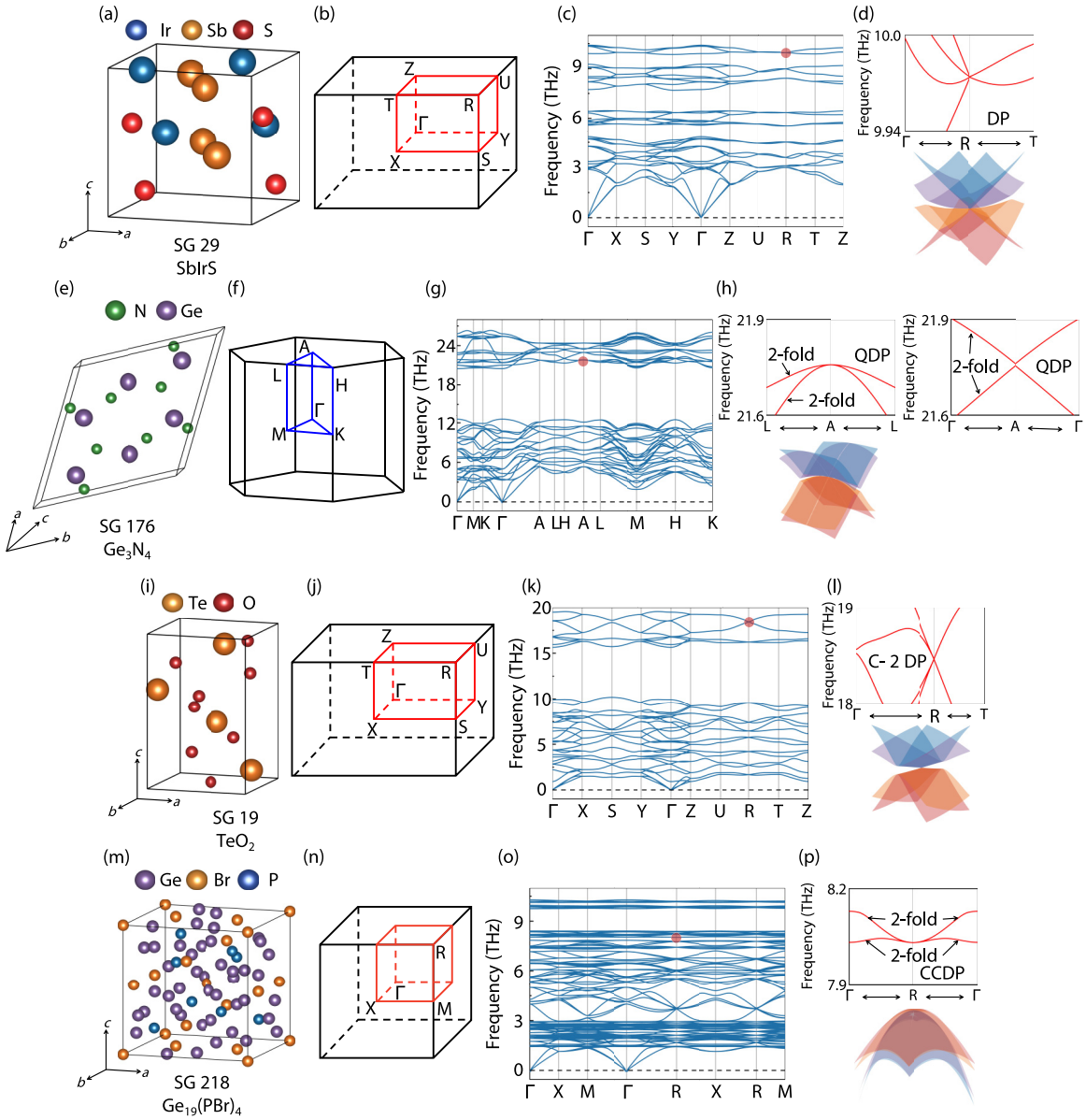

FIG. 6. [(a), (e), (i), and (m)] Crystal structures for the SbIrS, Ge_3N_4, TeO_2, and $Ge_{19}(PBr)_4$, respectively. [(b), (f), (j), and (n)] 3D BZs for the SbIrS, Ge_3N_4, TeO_2, and $Ge_{19}(PBr)_4$, respectively. [(c), (g), (k), and (o)] Phonon dispersions for the SbIrS, Ge_3N_4, TeO_2, and $Ge_{19}(PBr)_4$, respectively. [(d), (h), (i), and (p)] Enlarged phonon curves along the $\Gamma - R - T$ (for SbIrS), $L - A - L$, and $\Gamma - A - \Gamma$ (for Ge_3N_4), $\Gamma - R - T$ (for TeO_2), and the $\Gamma - R - \Gamma$ (for $Ge_{19}(PBr)_4$) paths, respectively, and the 3D plots of the phonon bands around the DP at the R (for SbIrS) in the $k_x - k_y$ plane, QDP at the A (for Ge_3N_4) in the $k_x - k_y$ plane, C-2 DP at the R (for TeO_2) in the $k_x - k_y$ plane, CCDP at the R [for $Ge_{19}(PBr)_4$] point in the plane normal to the $k_{(111)}$ path, respectively.

at the R point [see Figs. 6(k) and 6(l)]. We then understand the physics of the C-2 DP phonons in TeO_2 via the following. For point R of space group No. 19, crystal symmetry guarantees the existence of a 2D IRR (R1), which corresponds to a WP. $\mathcal{T}$ can enforce two WPs of the same chirality to appear at the same point and form C-2 DP (4D IRR R1R1). Under the basis of R_1R_1, the matrix representations of generating elements and $\mathcal{T}$ are given by $C_{2z} = i\Gamma_{0,2}$, $C_{2y} = i\Gamma_{0,1}$, and $\mathcal{T} = -\Gamma_{2,2}$.

The effective Hamiltonian based on the symmetry constraints can be written by

$$\mathcal{H}_R^{19} = c_1\Gamma_{0,0} + c_2\Gamma_{0,3}k_x + c_3\Gamma_{0,1}k_y + c_4\Gamma_{0,2}k_z. \quad (11)$$

The effective Hamiltonian $\mathcal{H}_R^{19}$ describes a C-2 DP with linear dispersion, which also is confirmed by our calculations. Moreover, the phonon LDOS projected on the (100) surface is shown in Fig. S1(c) (see Ref. [98]). The white arrows indicate the phonon surface states. Also, the constant frequency slice at 18.5 THz is given in Fig. S1(d) (see Ref. [98]). Corresponding to the obtained $\mathcal{C}$ of the C-2 DPP, as expected, double arc-shaped surface states are emanating from the projection of the C-2 DPP (i.e., $\bar{R}$ point).

For the CCDP, it is a 0D fourfold band degeneracy with a topological charge $\mathcal{C} = 0$. It is formed by a cubic crossing between two doubly degenerate bands along a certain

high-symmetry line and has a quadratic band splitting in the plane normal to the high-symmetry line. As shown in Figs. 6(o) and 6(p), one finds that the semiconductor $Ge_{19}(PBr)_4$ [99] is a candidate with CCDP at the R point, and this CCDP shows a cubic crossing formed by two doubly degenerate bands (Nos. 137, 138 and Nos. 135, 136) along the $k_{(111)}$ path (i.e., $\Gamma - R$ path) and a quadratic band splitting in the plane normal to $k_{(111)}$ path [see Fig. 6(p)]. We then understand the physics of the CCDP phonons in $Ge_{19}(PBr)_4$ via the following: The DP at the R is supported by 4D IRR (R_3R_3) of the $P\bar{4}3n$ SG (No. 218). Under the basis of R_3R_3, the matrix representations of generating elements and $\mathcal{T}$ are given by $S_{4x}^{+} = \frac{\sqrt{3}i}{2}\Gamma_{0,1} - \frac{i}{2}\Gamma_{0,2}$, $\sigma_{da} = i\Gamma_{0,2}$ $C_{33}^{-} = -\frac{1}{2}\Gamma_{0,0} + \frac{\sqrt{3}i}{2}\Gamma_{0,3}$, and $\mathcal{T} = -\Gamma_{2,2}$. The effective Hamiltonian up to the third order based on the symmetry constraints can be written as

$$\begin{aligned}\mathcal{H}_R^{218} = &(c_1 + c_2k^2)\Gamma_{0,0} + \sqrt{3}(c_3\Gamma_{3,1} + c_4\Gamma_{1,1} + c_5\Gamma_{2,1})\\ &\times \left(k_x^2 - k_y^2\right) - (c_3\Gamma_{3,2} + c_4\Gamma_{1,2} + c_5\Gamma_{2,2})\\ &\times \left(k_x^2 + k_y^2 - 2k_z^2\right) + (c_6\Gamma_{1,0} + c_7\Gamma_{2,0} + c_8\Gamma_{3,0})\\ &\times k_xk_yk_z. \end{aligned} \tag{12}$$

The dispersion characteristic of Hamiltonian $\mathcal{H}_R^{218}$ shows that band crossing at the R is a CCDP, and our calculations also confirm this fact.

VIII. TP, C-2 TP, QTP, AND QCTP PHONONS IN SOME SEMICONDUCTORS

Threefold degeneracy point phonons can be divided into four parts [70], TP, C-2 TP, QTP, and QCTP, respectively. Note that, as mentioned in Ref. [56], TP phononic materials have gapless topological phonon modes that can provide additional scattering channels in the three phonon-phonon scattering processes to decrease the mean free path and suppress κ_l.

In this section, we would like to point out that all four types of threefold degeneracy point phonons can be found in the phonon curves of semiconductors. For the TP, it is a 0D threefold band degeneracy formed by a linear crossing between a doubly degenerate band and a nondegenerate band. The TP does not have a well-defined topological charge of Chern number, as there does not exist a fully gapped sphere surrounding TP in BZ. Figure 7(c) shows that a TP appears on the $\Gamma - R$ path in the frequency region around 3.0 THz of the $MgTe_2$ semiconductor [100]. For clarity, the phonon branches Nos. 18–20 along the $\Gamma - R$ path and the 3D plot of the TP are shown in Fig. 7(d). One may understand the appearance of TP phonons in $MgTe_2$ semiconductor based on the followings. The TP on the $\Gamma - R$ path is formed by a linear crossing between 2D IRRs $\Lambda_2 \oplus \Lambda_3$ and a 1D IRR Λ_1 [see Fig. 7(d)]. Under the basis of $\{\Lambda_1, \Lambda_2 \oplus \Lambda_3\}$, the matrix representations of generating elements and antiunitary operator are given by

$$C_{31}^{+} = \begin{pmatrix} 1 & 0 & 0 \\ 0 & -\frac{1}{2} + \frac{\sqrt{3}}{2}i & 0 \\ 0 & 0 & -\frac{1}{2} - \frac{\sqrt{3}}{2}i \end{pmatrix}, \mathcal{IT} = \begin{pmatrix} 1 & 0 & 0 \\ 0 & 0 & 1 \\ 0 & 1 & 0 \end{pmatrix}. \tag{13}$$

The effective Hamiltonian based on the symmetry constraints can be written as

$$\mathcal{H}_{\Gamma\text{-}R}^{205} = \begin{pmatrix} c_1 + \frac{4\sqrt{3}}{3}c_3q_z + c_2(q_z - c_4q_y) & (c_4 - ic_5)(q_x - iq_y) & c_4q_x + ic_5q_x - c_5q_y \\ (c_4 + ic_5)(q_x + iq_y) & c_1 - \frac{2\sqrt{3}}{3}c_3q_z + c_2(q_z + c_4q_y) & (c_6 - ic_7)(q_x - iq_y) \\ c_4 - ic_5q_x - c_5q_y & (c_6 + ic_7)(q_x + iq_y) & c_1 + c_2q_z - \frac{2\sqrt{3}}{3}c_3q_z \end{pmatrix}. \tag{14}$$

Here, $q_x = \frac{1}{\sqrt{6}}(-k_x - k_y + 2k_z)$, $q_y = \frac{1}{\sqrt{2}}(k_x - k_y)$, and $q_z = \frac{1}{\sqrt{3}}(k_x + k_x + k_z)$. The Hamiltonian $\mathcal{H}_{\Gamma\text{-}R}^{205}$ describes a TP with linear dispersion along the $\Gamma - R$ path.

For the C-2 TP, it is a 0D threefold band degeneracy with a topological charge $\mathcal{C} = \pm 2$. It features a linear splitting along any direction in momentum space. As shown in Figs. 7(g) and 7(h), a C-2 TP, located around the frequency of 10 THz and formed by phonon branches Nos. 26–28 can be found at the Γ point in the phonon curves of the semiconductor ZrSO [101].

The appearance of the C-2 TP at the Γ arises from the essential band degeneracy, which is protected by 3D IRR Γ_4 of the T little group. Under the basis of Γ_4, the matrix representations of generating elements and time-reversal symmetry $\mathcal{T}$ are given by

$$C_{31}^{+} = \begin{pmatrix} 0 & 0 & 1 \\ 1 & 0 & 0 \\ 0 & 1 & 0 \end{pmatrix}, \quad C_{2z} = \begin{pmatrix} -1 & 0 & 0 \\ 0 & -1 & 0 \\ 0 & 0 & 1 \end{pmatrix}, \quad C_{2y} = \begin{pmatrix} -1 & 0 & 0 \\ 0 & 1 & 0 \\ 0 & 0 & -1 \end{pmatrix}, \quad \mathcal{T} = \frac{-\sqrt{3}i - 1}{2}\begin{pmatrix} 1 & 0 & 0 \\ 0 & 1 & 0 \\ 0 & 0 & 1 \end{pmatrix}. \tag{15}$$

As a consequence, the effective Hamiltonian around the Γ point could be derived as

$$\mathcal{H}_{\Gamma}^{198} = \begin{pmatrix} c_1 & -ic_2k_z & ic_2k_y \\ ic_2k_z & c_1 & -ic_2k_x \\ -ic_2k_y & ic_2k_x & c_1 \end{pmatrix}. \tag{16}$$

The Hamiltonian $\mathcal{H}_{\Gamma}^{198}$ describes a standard C-2 TP with linear dispersion at the Γ point. The phonon LDOS and the frequency slice corresponding to the (001) surface at 9.9 THz are shown in Fig. S2 of Ref. [98], in which the double arc-shaped surface states are obvious.

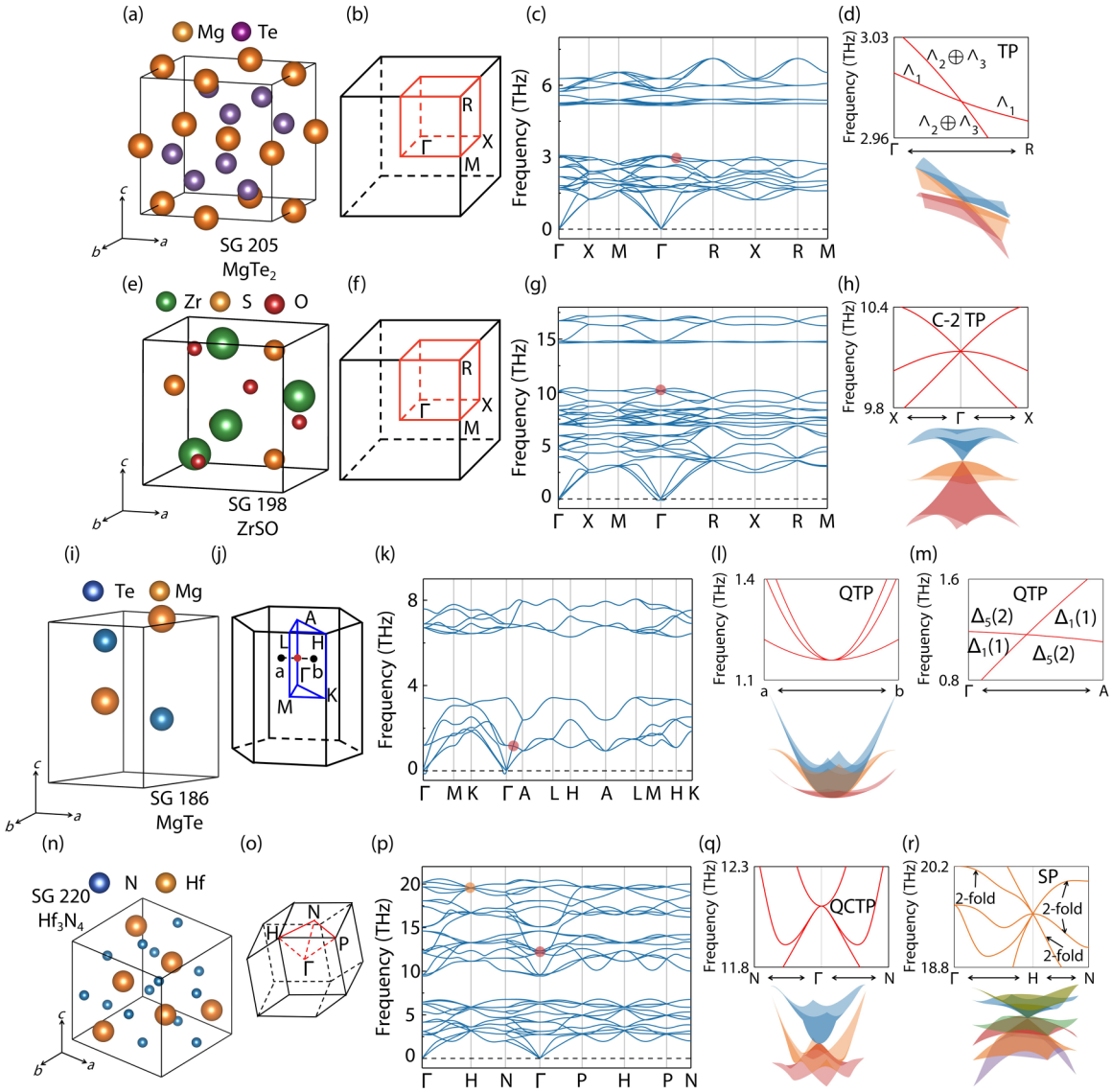

FIG. 7. [(a), (e), (i), and (n)] Crystal structures for the $MgTe_2$, ZrSO, MgTe, and Hf_3N_4, respectively. [(b), (f), (j), and (o)] 3D BZs for the $MgTe_2$, ZrSO, MgTe, and Hf_3N_4, respectively. [(c), (g), (k), and (p)] Phonon dispersions for the $MgTe_2$, ZrSO, MgTe, and Hf_3N_4, respectively. (d) Enlarged phonon curves along the $\Gamma - R$ path and the 3D plot of phonon bands around the TP in the $k_x - k_y$ plane for $MgTe_2$. (h) Enlarged phonon curves along the $X - \Gamma - X$ paths and the 3D plot of phonon bands around the C-2 TP at the Γ point in the $k_x - k_y$ plane for ZrSO. [(l) and (m)] Enlarged phonon curves along the $a - b$ and $\Gamma - A$ paths and the 3D plot of phonon bands around the QTP in the $k_x - k_y$ plane for MgTe. [(q) and (r)] Enlarged phonon curves along the $N - \Gamma - N$ paths, the $\Gamma - H - N$ paths, and the related 3D plots of the phonon bands around the QCTP at the Γ and the SP at the H points in the $k_x - k_y$ plane for Hf_3N_4.

The QTP also does not have a well-defined topological charge of the Chern number (as is the case with TP). However, in contrast to TP hosts a linear band splitting along any direction in momentum space, QTP features a quadratic band splitting in the plane normal to the high-symmetry line. In Figs. 7(i)–7(m), we show that the QTP, located around the frequency of 1.2 THz, can be found in the phonon curves of semiconductor MgTe [102] on the $\Gamma - A$ path. From Figs. 7(l) and 7(m), one finds that the phonon branches around the QTP host a linear band dispersion on the Γ-A path, and a quadratic band splitting in the plane normal to the $\Gamma - A$ path. One may understand the appearance of QTP phonons in MgTe semiconductor based on the following: The QTP on the $\Gamma - A$ path is formed by a band crossing between a 2D IRR Δ_5 and a 1D IRR Δ_1 [see Fig. 7(m)]. Under the basis of $\{\Delta_1, \Delta_5\}$, the matrix representations of generating elements and antiunitary operator are given by

$$C_6^+ = \begin{pmatrix} 1 & 0 & 0 \\ 0 & -\frac{1}{2} & -\frac{\sqrt{3}}{2} \\ 0 & \frac{\sqrt{3}}{2} & -\frac{1}{2} \end{pmatrix}, \quad \sigma_{v1} = \begin{pmatrix} 1 & 0 & 0 \\ 0 & 1 & 0 \\ 0 & 0 & -1 \end{pmatrix}. \quad (17)$$

The effective Hamiltonian based on the symmetry constraints can be written as

$$\mathcal{H}^{186}_{\Gamma\text{-}A} = \begin{pmatrix} c_1 + c_5\left(k_x^2 + k_y^2\right) + c_3 k_z + c_8 k_z^2 & \alpha\left(k_x^2 - k_y^2\right) & \alpha k_x k_y \\ \alpha^*\left(k_x^2 - k_y^2\right) & c_2 + c_6\left(k_x^2 + k_y^2\right) + c_7 k_y^2 + c_4 k_z + c_9 k_z^2 & c_7 k_x k_y \\ \alpha^* k_x k_y & c_7 k_x k_y & c_2 + c_6\left(k_x^2 + k_y^2\right) + c_7 k_x^2 + c_4 k_z + c_9 k_z^2 \end{pmatrix}. \tag{18}$$

Where c_i are real parameters and α is a complex parameter. The Hamiltonian $\mathcal{H}^{186}_{\Gamma\text{-}A}$ describes a QTP along the $\Gamma - A$ path, and the result is also confirmed by our calculations.

The QCTP is a 0D threefold band degeneracy with a topological charge $\mathcal{C} = 0$ and features a quadratic band splitting along any direction in momentum space. As shown in Figs. 7(n)–7(r), we show the semiconductor Hf_3N_4 [103] hosts QCTP at the Γ point [see Fig. 7(q)] and the SP at the H point [see Fig. 7(r)].

The appearance of the QCTP at the Γ arises from the essential band degeneracy, which is protected by 3D IRR Γ_4 of T_d little group. Under the basis of Γ_4, the matrix representations of generating elements and time-reversal symmetry are given by

$$C_{31}^- = \begin{pmatrix} 0 & 1 & 0 \\ 0 & 0 & 1 \\ 1 & 0 & 0 \end{pmatrix}, \quad C_{2z} = \begin{pmatrix} -1 & 0 & 0 \\ 0 & -1 & 0 \\ 0 & 0 & 1 \end{pmatrix}, \quad C_{2x} = \begin{pmatrix} 1 & 0 & 0 \\ 0 & -1 & 0 \\ 0 & 0 & -1 \end{pmatrix},$$
$$\sigma_{da} = \begin{pmatrix} 0 & -1 & 0 \\ -1 & 0 & 0 \\ 0 & 0 & 1 \end{pmatrix}, \quad \mathcal{T} = \frac{-\sqrt{3}i - 1}{2} \begin{pmatrix} 1 & 0 & 0 \\ 0 & 1 & 0 \\ 0 & 0 & 1 \end{pmatrix}. \tag{19}$$

The effective Hamiltonian based on the symmetry constraints can be written as

$$\mathcal{H}^{220}_{\Gamma} = \begin{pmatrix} c_1 + c_2 k^2 + c_3\left(2k_x^2 - k_y^2 - k_z^2\right) & c_4 k_x k_y & c_4 k_x k_z \\ c_4 k_x k_y & c_1 + c_2 k^2 - c_3\left(k_x^2 - 2k_y^2 + k_z^2\right) & c_4 k_y k_z \\ c_4 k_x k_z & c_7 k_x k_y & c_1 + c_2 k^2 - c_3\left(k_x^2 + k_y^2 - 2k_z^2\right) \end{pmatrix}, \tag{20}$$

where $k = \sqrt{k_x^2 + k_y^2 + k_z^2}$, and one can find that the Hamiltonian $\mathcal{H}^{220}_{\Gamma}$ exhibits quadratic band dispersion along any direction.

IX. SP PHONONS IN SOME SEMICONDUCTORS

The SP is a 0D sixfold band degeneracy with a topological charge $\mathcal{C} = 0$. It features a linear band splitting along any direction in momentum space. Compared to the electronic structures, the phonon curves are an excellent platform to realize the spinless degenerate phonons with the maximum fold (i.e., spinless SP phonons) due to the following reasons: (1) Almost all the SP states proposed in electronic systems usually are far from the Fermi level [104,105]. However, the Pauli exclusion principle does not apply to SP phonon systems. (2) Owing to the effect of spin-orbital coupling, the spinless SP states are usually gapped in electronic systems. However, phonon systems without spin-orbital coupling effect can be viewed as a viable platform for investigating ideal spinless sixfold emergent particles.

As mentioned in Sec. VIII, one finds that the SP can be found at the H point in the phonon curves of semiconductor Hf_3N_4 [103] [see Fig. 7(r)]. One can understand the exitance of the SP phonons in Hf_3N_4 with the help of symmetry analysis as follow. The SP with sixfold degeneracy cannot be formed relying solely on crystalline symmetries. And an antiunitary operation like $\mathcal{T}$ is necessary for the formation of 6D IRR of the little cogroup. The SP at the H point in Hf_3N_4 is enforced by 6D IRR H_4H_5, and under the basis of H_4H_5, the matrix representations of generating elements and time-reversal symmetry are given by

$$C_{2x} = A_1 \oplus A_1, \quad A_1 = \begin{pmatrix} 1 & 0 & 0 \\ 0 & 1 & 0 \\ 0 & 0 & -1 \end{pmatrix}, \quad C_{2y} = A_2 \oplus A_2,$$
$$A_2 = \begin{pmatrix} 1 & 0 & 0 \\ 0 & -1 & 0 \\ 0 & 0 & 1 \end{pmatrix}, \quad C_{31}^+ = A_3 \oplus A_3, \quad A_3 = \begin{pmatrix} 0 & 1 & 0 \\ 0 & 0 & -1 \\ -1 & 0 & 0 \end{pmatrix},$$
$$S_{4x}^- = -A_4 \oplus A_4, \quad A_4 = \begin{pmatrix} 0 & i & 0 \\ -i & 0 & 0 \\ 0 & 0 & i \end{pmatrix}, \quad \mathcal{T} = \sigma_x \otimes A_0, A_0 = \begin{pmatrix} 1 & 0 & 0 \\ 0 & 1 & 0 \\ 0 & 0 & 1 \end{pmatrix}. \tag{21}$$

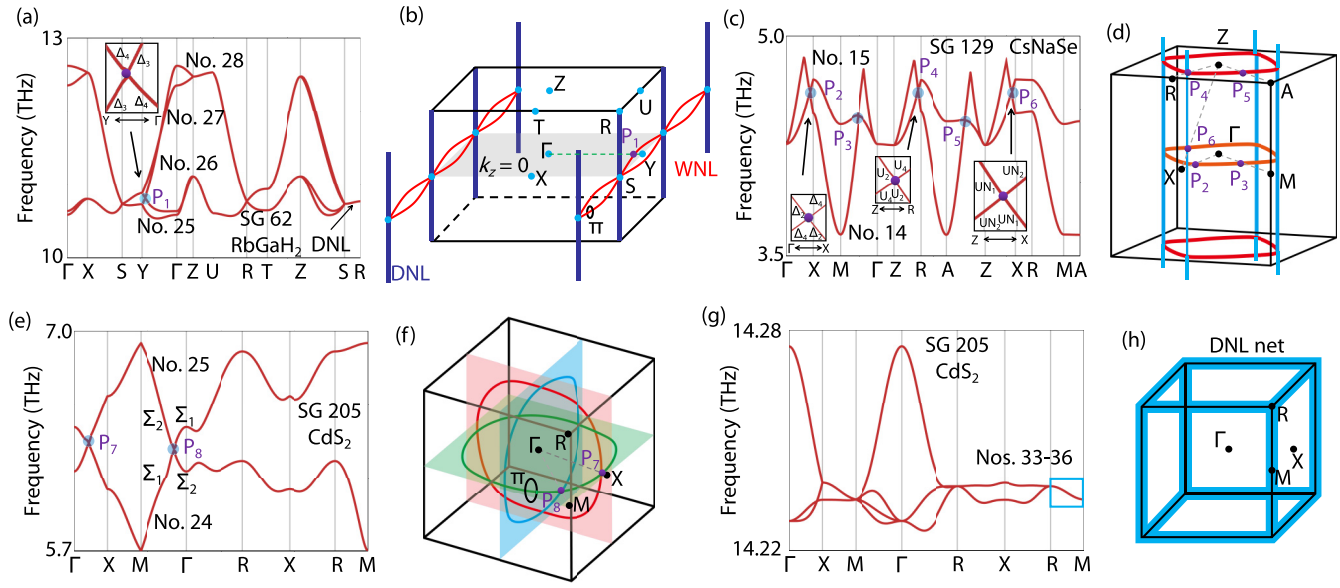

FIG. 8. [(a), (c), (e), and (g)] Enlarged phonon curves for the $RbGaH_2$, CsNaSe, and CdS_2. [(b), (d), (f), and (h)] Schematic diagrams for the DNL and WNL phonons, open and closed nodal line phonons, nodal link phonons, and DNL net phonons in $RbGaH_2$, CsNaSe, and CdS_2, respectively. Note that the nontrivial nodal lines will possess a quantized π Berry phase.

As a consequence, the effective Hamiltonian around the H point could be derived as

$$\mathcal{H}_H^{220} = \begin{pmatrix} H_{11} & H_{12} \\ H_{21} & H_{22} \end{pmatrix}, \tag{22}$$

with

$$H_{11} = \begin{pmatrix} c_1 & -k_x c_2 & k_y c_2 \\ -k_x c_2 & c_1 & k_z c_2 \\ k_y c_2 & k_z c_2 & c_1 \end{pmatrix},$$
$$H_{22} = \begin{pmatrix} c_1 & k_x c_2 & -k_y c_2 \\ k_x c_2 & c_1 & -k_z c_2 \\ -k_y c_2 & -k_z c_2 & c_1 \end{pmatrix},$$
$$H_{12} = \begin{pmatrix} 0 & \alpha k_x & \alpha k_y \\ -\alpha k_x & 0 & -\alpha k_z \\ -\alpha k_y & \alpha k_z & 0 \end{pmatrix},$$
$$H_{21} = \begin{pmatrix} 0 & -\alpha^* k_x & -\alpha^* k_y \\ \alpha^* k_x & 0 & \alpha^* k_z \\ \alpha^* k_y & -\alpha^* k_z & 0 \end{pmatrix}. \tag{23}$$

Here, c_i are real parameters and α is a complex parameter. The Hamiltonian $\mathcal{H}_H^{220}$ describes a SP at the H point, and the result is also confirmed by our calculations.

X. NL PHONONS IN SOME SEMICONDUCTORS

A. WNL and DNL phonons in some semiconductors

A node is often defined by the number of degeneracies. The Weyl point is the doubly degenerate point that fulfills the Weyl model. The Dirac point is the fourfold degenerate point that fulfills the Dirac model. The phrases Weyl and Dirac can also be used to describe the nodal line's degeneracy. That is, the Weyl nodal line (WNL) is the twofold degenerate nodal line, whereas the Dirac nodal line (DNL) is the fourfold degenerate nodal line (DNL).

Here, we would like to point out that the WNL and the DNL could coexist in the phonon curves of the semiconductor $RbGaH_2$ [106] with SG. 62. The enlarged phonon branches (with Nos. 25–28) are shown in Fig. 8(a). From Fig. 8(a), one finds an obvious twofold degenerate crossing point on the $Y - \Gamma$ path, and such crossing point belongs to twofold degenerate WNLs in the 3D BZ [see the red lines in Fig. 8(b)]. Moreover, the four phonon branches (Nos. 25–28) degenerated into a fourfold degenerate nodal line, i.e., Dirac line, along the $S - R$ path [see the blue lines in Fig. 8(b)]. One can understand the deeper physics for the WNL and DNL phonons in $RbGaH_2$ based on the symmetry analysis as follows: The generators of the little group of the $S - R$ path are $\widetilde{C}_{2z} = \{C_{2z} \mid \frac{1}{2}0\frac{1}{2}\}$ and $\widetilde{M}_y = \{M_y \mid 0\frac{1}{2}0\}$. Considering the algebraic relationship between these operations and $\mathcal{T}$, a quadruple degenerate state can be formed, whose IRR is Q_1Q_1. Based on the quartet basis, the matrix representations of the generators can be expressed as

$$C_{2z} = \sigma_0 \otimes \sigma_z, \quad M_y = \sigma_z \otimes \sigma_x, \quad C_{2y}\mathcal{T} = i\sigma_y \otimes \sigma_0. \tag{24}$$

The effective Hamiltonian based on the symmetry constraints can be written as

$$\mathcal{H}_{\text{S-R}}^{62} = (c_1 + c_2 k_z) + \begin{pmatrix} H_D & H_{12} \\ H_{12}^\dagger & H_D \end{pmatrix}, \tag{25}$$

with

$$H_D = c_3 k_x \sigma_x + c_4 k_y \sigma_y, \quad H_{12} = \alpha k_x \sigma_y + \beta k_y \sigma_x. \tag{26}$$

Here, c_i are real parameters, and α, β are complex parameters. The Hamiltonian $\mathcal{H}_{\text{S-R}}^{62}$ describes a DNL along the $S - R$ path. In addition, the formation of WNL in the $k_z = 0$ plane is protected by the glide mirror symmetry with different eigenvalues.

B. Open and closed nodal line phonons in some semiconductors

Moreover, the nodal line phonons can be divided into open and closed nodal line phonons from a mathematical perspective. The BZ can be the topological equivalent to a 3D torus $\mathbb{T}^3$. Closed lines on $\mathbb{T}^3$ can be classified under its fundamental homotopy group $\pi_1(\mathbb{T}^3) = Z^3$, labeled by three integers. Each integer shows the number of times the line passes around one of the three directions. Hence, the closed nodal line (without traversing through the BZ) should be in a class with $Z^3 : (0, 0, 0)$; however, for the open nodal line (traverses once in the z direction) should be in a class with (0,0,1).

From Fig. 8(c), we show the open and closed nodal lines coexist in the phonon curves of serriconductor CsNaSe [107]. The crossing points on the $\Gamma - X$ and $\Gamma - M$ belong to the closed nodal lines on the $k_z = 0$ plane, and the crossing points on the $Z - R$ and $Z - A$ paths belong to the closed nodal lines on the $k_z = \pm\pi$ planes. However, the crossing point on the $Z - X$ path belongs to the open nodal lines, which traverse once in the z direction.

One can understand the appearance of the closed nodal lines on the $k_z = 0$ and $k_z = \pm\pi$ planes, and the open nodal lines along the z direction from the symmetry analysis: The little group of the $\Gamma - X$ path is C_{2v}, which contains two mirrors operator M_x and M_z. The calculated IRRs of two crossing bands of the $\Gamma - X$ path are Δ_2 and Δ_4 [see Fig. 8(c)], and the corresponding M_x eigenvalues are 1 and -1, so that a nodal line can be formed in the $k_x = 0$ plane. Considering the $\widetilde{C}_{4z}$ symmetry of the system, there are four such nodal lines. On the other hand, the $\Gamma - X$ path is also shared by $k_z = 0$ plane, and the eigenvalues of M_z associated with IRRs Δ_2 and Δ_4 are also opposite, so the crossing point of $\Gamma - X$ path will also form a mirror-protected nodal line in $k_z = 0$ plane. The same analysis is applied to the $Z - R$ path, and these nodal lines together form a nodal cage.

C. NL phonons with different shapes in some semiconductors

If there is more than one nodal line/ring in momentum space, these nodal line/ring phonons can combine to form complex topological nodal structures [48]. Here, we would like to point out that the nodal link phonons, DNL net phonons, WNL net phonons, nodal box phonons, nodal chain phonons, and nodal cage phonons can be found in the phonon curves of semiconductors.

As shown in Fig. 8(e), one finds that there are two crossing points on the $\Gamma - X$ and Γ-M paths in the phonon curves of semiconductor CdS_2 [108] with SG 205, and such two crossing points belong a closed nodal line on the $k_x = 0$ plane. Note that the closed nodal lines can also appear on the $k_y = 0$ and $k_z = 0$ planes, and these three closed nodal lines tend to form a nodal link [109,110] in the 3D BZ [see Fig. 8(f)].

The lattice of CdS_2 has the SG symmetry of $Pa\bar{3}$ (No. 205), whose point group T_h contains three mirror operators M_x, M_y, and M_z. Taking M_z symmetry as an example, if a band inversion occurs in bands with the opposite M_z eigenvalues on the M_z-invariant plane [see IRRs in Fig. 8(e)], a nodal line is formed. It is worth noting that these three mirrors belong to the same conjugate class of the T_h group, which causes nodal lines to appear on the other two mirror invariant planes (M_x and M_y) and a nodal link is formed.

As shown in Fig. 8(g), one finds that the Nos. 33–36 phonon branches merged into a fourfold degenerate band on the $R - M$ path in the phonon curves of semiconductor CdS_2. Such fourfold degenerate bands belong to the DNL. As shown in Fig. 8(h), a DNL net [111] can be observed in the 3D BZ.

The generators of little group of the $R - M$ path are $\widetilde{C}_{2z} = \{C_{2z} \mid \frac{1}{2}, 0, \frac{1}{2}\}$ and $\widetilde{M}_x = \{M_x \mid \frac{1}{2}, \frac{1}{2}, 0\}$. Considering the algebraic relationship between these operations and $\mathcal{T}$, a quadruple degenerate state T_1T_1 can be formed. Based on the quartet basis, the matrix representations of the generators can be expressed as

$$C_{2z} = \Gamma_{0,2}, \quad M_x = -i\Gamma_{0,1}, \quad \text{and} \quad \mathcal{IT} = -\Gamma_{2,2}. \tag{27}$$

The effective Hamiltonian based on the symmetry constraints can be written as

$$\mathcal{H}^{205}_{\mathrm{R-M}} = (c_1 + c_2 k_z) + \sum_{i=1,2,3} (c_{i,1}\Gamma_{i,3}k_x + c_{i,2}\Gamma_{i,1}k_y). \tag{28}$$

The Hamiltonian $\mathcal{H}^{205}_{R\text{-}M}$ describes a DNL along the $R - M$ path.

As shown in Fig. 9(a), one finds that the twofold bands appear along the high-symmetry path $X - M$. Such twofold degenerate bands belong to the WNL. Figure 9(b) shows that the phonon dispersions of Au_2S in SG 224 [112] can form a square-shape WNL net in the first BZ.

The appearance of the WNL along the $X - M$ path arises from the essential band degeneracy, which is protected by 2D IRR Z_1. Under the basis of Z_1, the matrix representations of generating elements and time-reversal symmetry are given by

$$M_y = \sigma_y, \quad C_{2y} = \sigma_z, \quad \text{and} \quad \mathcal{IT} = -i\sigma_x. \tag{29}$$

As a consequence, the effective Hamiltonian could be derived as

$$\mathcal{H}^{224}_{X\text{-}M} = (c_1 + c_2 k_z)\sigma_0 + c_3\sigma_x k_y + c_4\sigma_y k_z. \tag{30}$$

The Hamiltonian $\mathcal{H}^{224}_{X\text{-}M}$ describes a WNL along the $X - M$ path. Considering other crystal symmetries, such WNL can form a square-shape nodal net.

As shown in Fig. 9(c), in the enlarged phonon curves of semiconductor Tl_2PtCl_6 [113]: one finds a crossing point on the $K - \Gamma$ path and a twofold degenerate band on the $\Gamma - L$ path. Note that the crossing point on the $K - \Gamma$ path is not isolated and belongs to the nodal line [see the blue line in Fig. 9(d)]. The twofold degenerate band on the $\Gamma - L$ path belongs to the WNLs [see the red lines in Fig. 9(d)]. The red nodal lines (along the $\Gamma - L$ path) and the blue nodal lines form a bow-tie-shaped nodal-line structure in the [011] mirror plane (see Fig. S3(e) in Ref. [98]). For the SG 225, it includes bow-tie-shaped nodal-line structures in these six mirror planes, i.e., [110], [101], [011], $[\bar{1}10]$, $[0\bar{1}1]$, and $[10\bar{1}]$ planes form a nodal box structure [114,115] as shown in Fig. 9(d).

The band degeneracy of the nodal box consists of two parts. The first part is the nodal line on the $\Gamma - L$ path, which originates from the essential 2D IRR Λ_3. Considering the symmetry of C_{4z}, there are four such nodal lines, constituting the four body diagonals of the nodal box. The second part

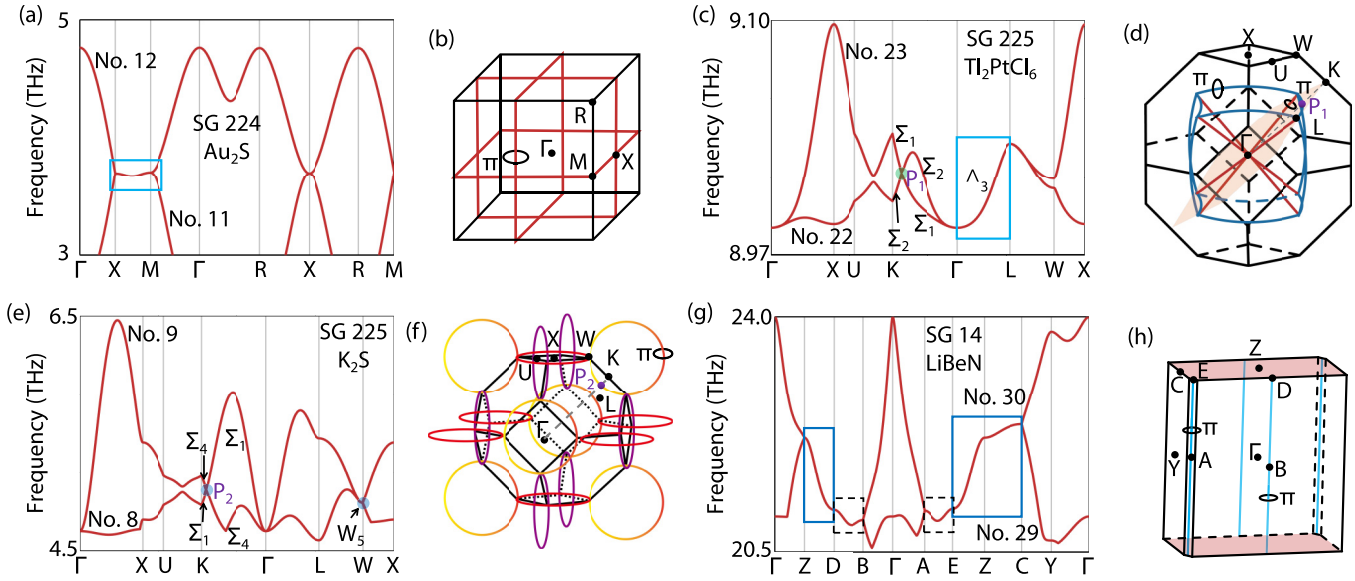

FIG. 9. [(a), (c), (e), and (g)] Enlarged phonon curves for the Au_2S, Tl_2PtCl_6, K_2S, and LiBeN, respectively. [(b), (d), (f), and (h)] Schematic diagrams for the WNL net phonons, nodal box phonons, nodal chain phonons, and nodal cage phonons in Au_2S, Tl_2PtCl_6, K_2S, and LiBeN semiconductors, respectively. Note that the nontrivial nodal lines will possess a quantized π Berry phase.

of the nodal box is protected by mirror symmetry. The IRRs of the band crossing point along the $\Gamma - K$ path are Σ_1 and Σ_2, which have opposite M_z eigenvalue ± 1. Therefore such band crossing point is not isolated and will form a nodal line on the M_z-invariant plane. Further considering the C_{4z} and C_3 rotation symmetries, such nodal lines would form the 12 edges of the nodal box.

As shown in Fig. 9(e), in the enlarged phonon curves of semiconductor K_2S with SG 225 [116], one finds two obvious crossing points, one is on the $K - \Gamma$ path, and the other is at the W point. These two crossing points belong to nodal lines (see the nodal lines in the $k_z = 0$ and $k_z = \pi$ planes from the DFT calculation in Figs. S4(e) and S4(f) of Ref. [98]).

The high-symmetry point W is shared by both the M_y and M_z-invariant plane. The calculated IRR of W point is W_5 [see Fig. 9(e)], and the corresponding character of M_y and M_z is zero, so these mirror operators have opposite mirror eigenvalues and can generate the nodal chain when W_5 is restricted to the little group of mirror-invariant plane. One can find that the IRRs of crossing bands along the $\Gamma - K$ path are Σ_1 and Σ_4, whose mirror eigenvalues are ± 1, thus protecting the stability of the nodal line. The dispersion of the nodal chain can be investigated by constructing the effective Hamiltonian based on the IRR of W_5. The effective Hamiltonian could be derived as

$$\mathcal{H}_{\mathrm{W}}^{225} = \left[c_1 + c_2 k_x^2 + c_3\left(k_y^2 + k_z^2\right)\right]\sigma_0 + \left[c_4 k_x + c_5\left(k_z^2 - k_y^2\right)\right]\sigma_x + c_6 k_y k_z \sigma_z. \quad (31)$$

The Hamiltonian $\mathcal{H}_{\mathrm{W}}^{225}$ hosts a linear band dispersion along k_x direction, and a quadratic band splitting in the other direction. Actually, the nodal lines in the 3D BZ can form a 3D chain network, as plotted in Fig. 9(f), and the W point of the 3D BZ should be the touching point. Figure 9(f) shows that nodal-chain phonons are running along all the k_i ($i = x$, y, and z) directions, resulting in a nodal chain structure [83,114] in the phonon curves of semiconductor K_2S.

As shown in Fig. 9(g), in the enlarged phonon curves of semiconductor LiBeN [117], one finds that the twofold degenerate bands appear on the $Z - D$, $D - B$, $A - E$, and $E - Z - C$ paths. For the twofold degenerate bands on the $Z - D$ and $E - Z - C$ paths, they belong to the nodal surface states on the $k_z = \pm\pi$ planes [see Fig. 9(h)]. However, the twofold degenerate bands on the $D - B$ and $A - E$ paths belong to the straight nodal lines in the 3D BZ [see the blue lines in Fig. 9(h)]. Combining the straight nodal lines and the nodal surfaces together can form a nodal cage structure [118,119] in the 3D BZ.

The lattice of LiBeN has the SG symmetry of $P2_1/c$ (No. 14), which have a twofold screw rotation $\widetilde{C}_{2y} = \{C_{2y} \mid 0, \frac{1}{2}, \frac{1}{2}\}$. The combination of twofold screw-rotation symmetry and time-reversal symmetry $\widetilde{C}_{2y}\mathcal{T}$ is antiunitary operator, which satisfies $(\widetilde{C}_{2y}\mathcal{T})^2 = -1$ on the $k_y = \pm\pi$ plane and lead to Kramers-like degeneracy of nodal surface. In addition, there are straight nodal lines with essential band degeneracy along the $D - B$ and $A - E$ paths whose IRRs are V_1V_2 and U_1U_2, respectively. These nodal lines and nodal surfaces together form the nodal cage structure.

XI. NS PHONONS IN SOME SEMICONDUCTORS

The nodal surface (NS) is a 2D degeneracy of twofold bands. The NS only emerges at the BZ boundary plane and has linear dispersion along the direction normal to the surface. Normally, the proposed NS phonons can be divided into three classes [70]: one-NS, two-NS, and three-NS phonons host one, two, and three pair(s) of NS states on the $k_i = \pm\pi$ ($i = x$, y, and z) planes. One may understand the formations of NS phonons based on the symmetry analyses as follows.

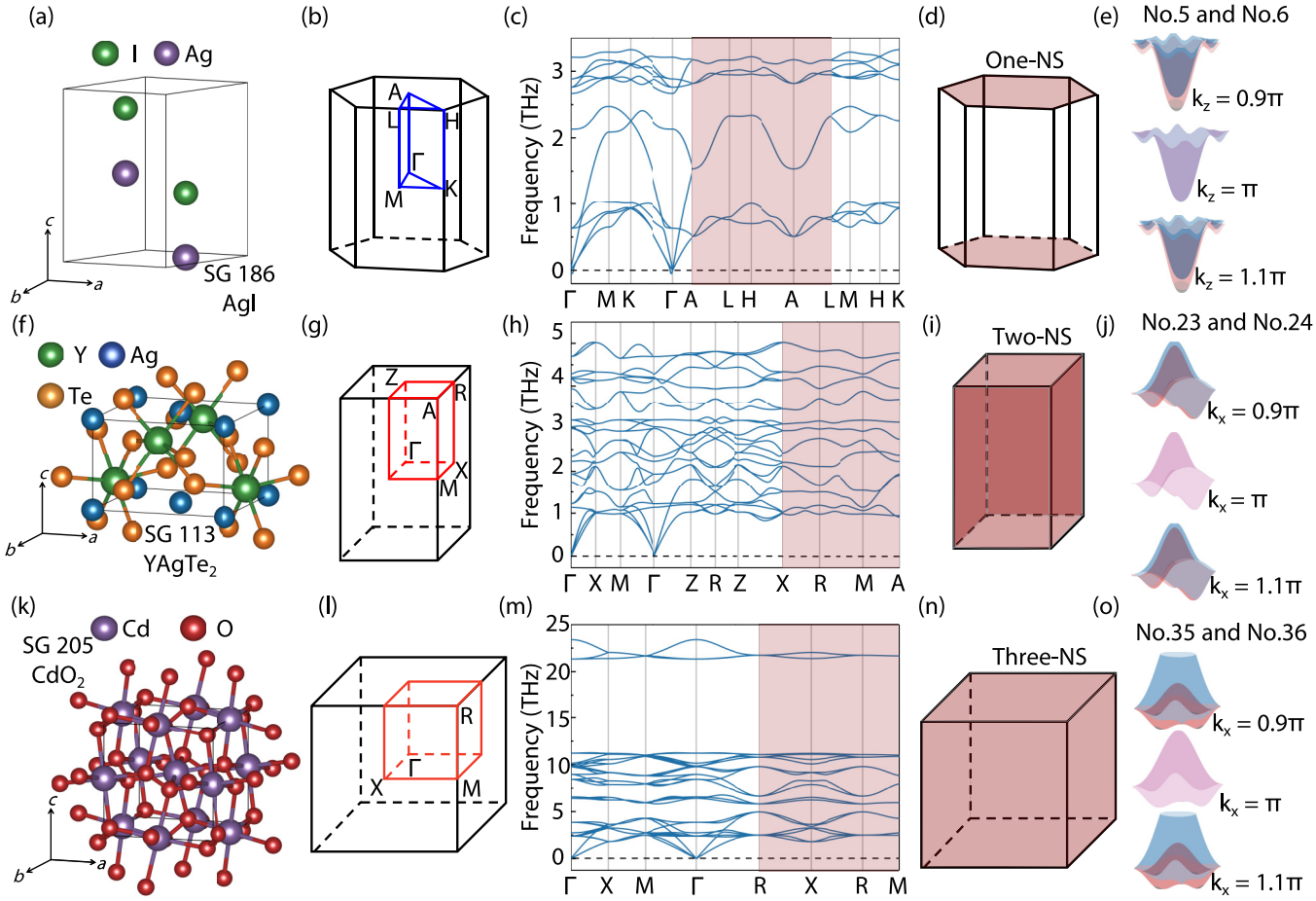

FIG. 10. [(a), (f), and (k)] Crystal structures for AgI, $YAgTe_2$, and CdO_2 semiconductors. [(b), (g), and (l)] 3D BZs for AgI, $YAgTe_2$, and CdO_2 semiconductors. [(c), (h), and (m)] Phonon dispersions for AgI, $YAgTe_2$, and CdO_2 semiconductors. [(d), (i), and (n)] Schematic diagrams for one-, two-, and three-NS phonons in AgI, $YAgTe_2$, and CdO_2 semiconductors. (e) 3D plots of the No. 5 and No. 6 phonon branches in the $k_z = 0.9\,\pi, \pi, 1.1\,\pi$ planes for AgI. (j) 3D plots of the No. 23 and No. 24 phonon branches in the $k_z = 0.9\,\pi, \pi, 1.1\,\pi$ planes for $YAgTe_2$. (o) 3D plots of the No. 35 and No. 36 phonon branches in the $k_z = 0.9\,\pi, \pi, 1.1\,\pi$ planes for CdO_2.

The nodal surfaces can be guaranteed by a combination of nonsymmorphic twofold screw-rotation symmetry and time-reversal symmetry $\widetilde{C}_{2i}\mathcal{T}(i = x, y, z)$, which satisfies $(\widetilde{C}_{2i}\mathcal{T})^2 = -1$ on the $k_i = \pm\pi$ plane and lead to the nodal surface. And the number of nodal surfaces depends on the number of twofold screw axis. For example, the space group of AgI is $P6_3mc$ (No. 186), which hosts only one twofold screw axis $\widetilde{C}_{2z} = \{C_{2z} \mid 0, 0, \frac{1}{2}\}$ and lead to one-NS [see Fig. 10(d)]. Similarly, the space group of YAgTe and CdO_2 contain two and three twofold screw axes, so they can host two-NS and three-NS, respectively [see Figs. 10(i) and 10(n)]. From Fig. 10(c), one finds that all the phonon bands along the A-L-H-A paths are twofold degeneracy for the AgI semiconductor [120], and therefore, these two phonon bands (Nos. 5 and 6) form one-NS phonons on the $k_z = \pm\pi$ planes [see Figs. 10(d) and 10(e)]. For clarity, from Fig. 10(e), one finds that the No. 5 and No. 6 phonon branches are not degenerate on the $k = 1.1\pi$ and 0.9π planes. From Fig. 10(h), one finds that the phonon bands for the $YAgTe_2$ semiconductor [121] doubly degenerate along the $X - R - M - A$ paths, resulting in the appearance of the two-NS phonons on the $k_x = \pm\pi$ and $k_y = \pm\pi$ planes [see Figs. 10(i) and 10(j)]. From Fig. 10(m), one finds that the phonon bands for the CdO_2 semiconductor [122] along the $R - X - R - M$ are twofold degenerate, reflecting the three-NS (or nodal wall) phonons on the $k_i = \pm\pi (i = x,\ y,\ \text{and}\ z)$ planes [see Figs. 10(n) and 10(o)].

XII. TOPOLOGICAL PHONONS IN SOME 2D SEMICONDUCTORS

Compared to 3D materials, 2D materials with less symmetrical constraints may more intuitively display the clean characteristics of topological phonons. Investigations of 2D topological phononic materials have been very limited [123–125]; here, we will show that three types of nodal point phonons can be found in 2D semiconductors.

The first type is the valley Weyl point (VWP) phonons in 2D semiconductors. In phonon systems, the Weyl point at a specific momentum point with a 2D IRR is called a VWP, and the possible effective Hamiltonian of VWP can be written as

$$\mathcal{H}_{\text{VWP}} = c_1(k_x\sigma_x + k_y\sigma_z). \tag{32}$$

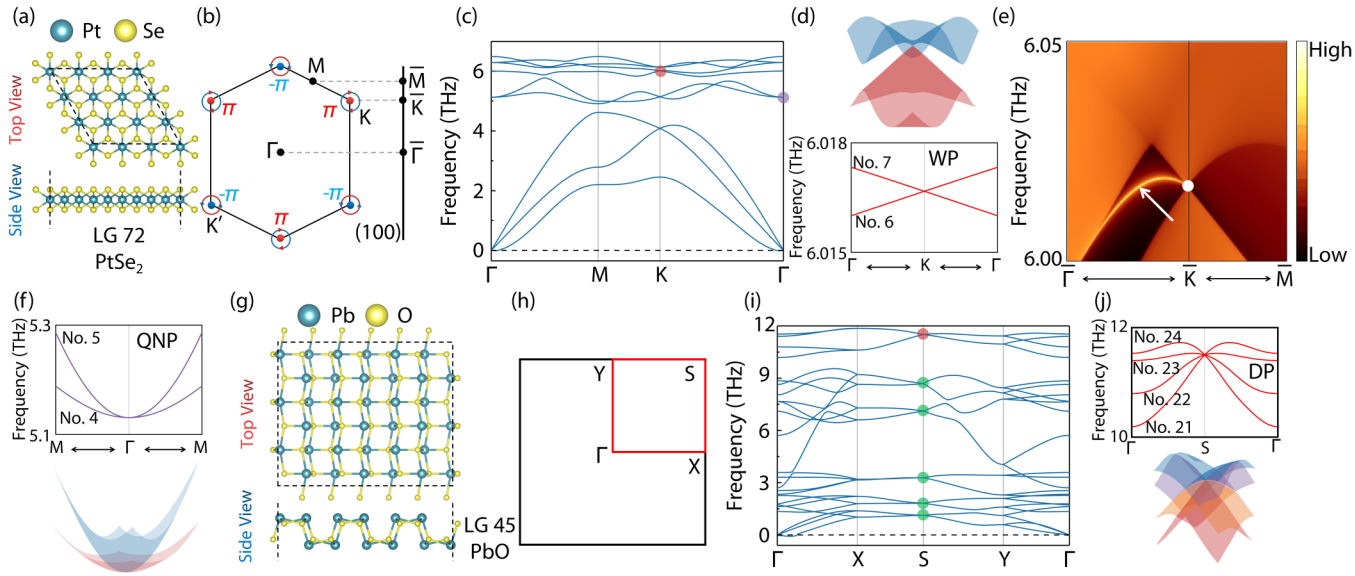

FIG. 11. (a) structural models for 2D monolayer $PtSe_2$ under different views. (b) 2D BZ, (100) edge state, and top view of Berry curvature distributions for LWP at the frequency around 6.01 THz. (c) phonon dispersion for 2D monolayer $PtSe_2$ and the LWP at the K point and QNP at the Γ point. (d) 3D plot of the No. 6 and No.7 phonon branches around the LWP at the point in the $k_x - k_y$ plane, and the enlarged phonon curves along the $\Gamma - K - \Gamma$ paths. (e) Edge states arising from the projections of the LWP. (f) the phonon curves (Nos. 4 and 5) along the $M - \Gamma - M$ paths, along with the 3D plot of the phonon branches around the QNP at the Γ point in the $k_x - k_y$ plane. (g) structural models for 2D monolayer PbO under different views. (h) 2D BZ for 2D monolayer PbO. (i) phonon dispersion for the 2D monolayer PbO and the DPs at the S point are shown by balls. (j) Enlarged phonon curves (Nos. 21–24) along the $\Gamma - S - \Gamma$ paths, and the 3D plot of the phonon branches around the DP [the one marked with a red ball in (i)] at the S point in the $k_x - k_y$ plane.

One can easily observe that the band dispersion is linear around the crossing point. Here, we select the 2D monolayer $PtSe_2$ [126], a semiconductor, as an example [see Fig. 11(a)] and show the VWP phonons located at the K and K' high-symmetry points [see Figs. 10(c) and 10(d)]. Moreover, the phonon Berry phases around the K' and K valleys are nontrivial and quantized with values of $-\pi$ and π, respectively [see Fig. 11(b)]. VWP phonons with nontrivial and quantized Berry phases will lead to a nontrivial topological edge state [see Fig. 11(e)].

The appearance of the VWP at the K arises from the essential band degeneracy, which corresponds to the 2D IRR of K_3. Under the basis of K_3, the matrix repres entations of generating elements are given by

$$C_3^+ = -\frac{1}{2}\sigma_0 - \frac{\sqrt{3}i}{2}\sigma_y, \quad C_{21}'' = \sigma_z, \quad \text{and} \quad \mathcal{IT} = \sigma_0. \tag{33}$$

The effective Hamiltonian based on the symmetry constraints can be written as

$$\mathcal{H}_K^{\mathrm{LG72}} = \begin{pmatrix} c_1 + c_2 k_y & c_2 k_x \\ c_2 k_x & c_1 - c_2 k_y \end{pmatrix}, \tag{34}$$

and $\mathcal{H}_K^{\mathrm{LG72}}$ describes a LWP at the K point.

Note that WPs with quadratic dispersion can also appear in 2D systems, namely, quadratic nodal points (QNPs). The minimum symmetry to enforce a QNP is the combination of time-reversal symmetry $\mathcal{T}$ and $C_{nz}(n = 3, 4, 6)$ rotational symmetry [127]. Therefore a QNP is usually located at the time-reversal invariant momenta, and the effective Hamiltonian of a QNP can be generally described by

$$\mathcal{H}_{\mathrm{QNP}} = \alpha k_-^2 \sigma_+ + \alpha^* k_+^2 \sigma_-. \tag{35}$$

Here, α is a complex parameter and $k_\pm = k_x \pm i k_y$, $\sigma_\pm = \sigma_x \pm \sigma_y$. This Hamiltonian reflects a quadratic dispersion for any direction. In Figs. 11(c) and 11(f), a QNP at the Γ point can also be found in the phonon curves of the 2D monolayer $PtSe_2$ around the frequency of the 5.2 THz.

The appearance of the QWP at the Γ arises from the essential band degeneracy, which corresponds to the 2D IRR of Γ_3^+. Under the basis of Γ_3^+, the matrix repres entations of generating elements are given by

$$\mathcal{I} = \sigma_0, \; C_3^+ = -\frac{1}{2}\sigma_0 + \frac{\sqrt{3}i}{2}\sigma_y, \; C_{21}'' = \sigma_z, \; \text{and} \; \mathcal{T} = \sigma_0. \tag{36}$$

The effective Hamiltonian based on the symmetry constraints can be written as

$$\mathcal{H}_\Gamma^{\mathrm{LG72}} = c_1 + c_2\left(k_x^2 + k_y^2\right) + \begin{pmatrix} c_3\left(k_x^2 - k_y^2\right) & -2c_3 k_x k_y \\ -2c_3 k_x k_y & -c_3\left(k_x^2 - k_y^2\right) \end{pmatrix}, \tag{37}$$

and $\mathcal{H}_\Gamma^{\mathrm{LG72}}$ describes a QNP at the Γ point.

Furthermore, 4D IRRs of the little cogroup emerging in the LGs can enforce the existence of Dirac point (DPs) at the HSPs in 2D systems. It is worth mentioning that the 4D IRs in the LGs are formed by sticking the two 2D IRs together by means of time-reversal symmetry $\mathcal{T}$. Thus these DPs usually occur at the TRIMs. The possible effective Hamiltonian around a DP can be described by

$$\mathcal{H}_{DP} = c_1 k_x \Gamma_{0,3} + c_2 k_y \Gamma_{1,0} + c_3 k_y \Gamma_{2,0} + c_4 k_y \Gamma_{3,0}, \tag{38}$$

where $c_i (i = 1, 2, 3, 4)$ is a real parameter, $\Gamma_{i,j} = \sigma_i \otimes \sigma_j$ with $i, j = 0, 1, 2, 3$. σ_0 is a 2×2 identity matrix, and $\sigma_{1,2,3} = \sigma_{x,y,z}$ are Pauli matrices. The DP in a 2D system exhibits linear band splitting along any direction. Here, as shown in Fig. 11(g), we select 2D PbO [128], a semiconductor, as an example to exhibit the DP at the S high-symmetry point in its phonon dispersion. The phonon dispersion is collected in Fig. 11(i), in which a series of fourfold degenerate DPs appear at the S high-symmetry point around different frequencies. For clarity, the enlarged phonon branches (Nos. 21–24) around the DP at the S point and the 3D plot of the phonon branches around the DP are shown in Fig. 11(j).

The appearance of the DP at the S arises from the essential band degeneracy, which corresponds to the 4D IRR of S_1S_2. Under the basis of S_1S_2, the matrix representations of generating elements are given by

$$C_{2x} = i\Gamma_{3,0},\ C_{2z} = \Gamma_{0,1},\ \mathcal{I} = \Gamma_{0,3},\ \text{and}\ \mathcal{T} = \Gamma_{1,0}. \quad (39)$$

The effective Hamiltonian based on the symmetry constraints can be written as

$$\mathcal{H}_s^{\text{LG45}} = c_1\Gamma_{0,0} + c_2\Gamma_{0,2}k_x + (c_3\Gamma_{1,2} + c_4\Gamma_{2,2})k_y, \quad (40)$$

and $\mathcal{H}_{\text{S}}^{\text{LG45}}$ describes indeed a linear DP at the S point.

XIII. CONCLUSIONS AND REMARKS

Based on first-principles calculations and symmetry analyses, a series of realistic semiconductors are proposed as candidates for hosting topological phonons. Almost all types of emergent particles, including Weyl points with different topological charges, single-pair-multi-Weyl points, single Weyl point with its nodal surface partner, various cases of Dirac points (DP, C-2 DP, QDP, CCDP), various cases of triple points (TP, C-2 TP, QTP, QCTP), sextuple points, nodal lines with different degenerates (WNL, DNL), nodal lines with different shapes (open and closed nodal lines, DNL net, WNL net, nodal link, nodal box, nodal chain, nodal cage), and one-, two-, and three-nodal surfaces can be observed in the phonon curves of semiconductors, indicating the pervasive presence of topological phonon modes in semiconductors.

Currently, the study of topological nodal phonons is in its infancy, driven primarily by academic curiosity. Nevertheless, these phonons may influence the observable properties or effects of matter in semiconductors. For example, Singh *et al.* [56] argued that phonon band crossings tend to introduce phonon-phonon scattering centers, which reduces the lattice thermal conductivity and may improve thermoelectric performance.

Different phonon surface modes, including the helicoid, double-helicoid, triple-helicoid, sextuple-helicoid surface modes can be found on the semi-infinite surfaces of the semiconductors. Zhang *et al.* [60] suggested that surface phonon modes may induce surface electronic structure anomalies via electron-phonon coupling. This could increase the likelihood of surface superconductivity. The visible surface phonon modes may also have potential applications in various phononic devices, such as phonon waveguides, thermal isolation, and theroelectrics, as mentioned by Li *et al.* [48] and Vasileiadis *et al.* [129]. Furthermore, most catalytic processes occur on the surfaces. Meng *et al.* [82] recently established a linear relationship between catalytic enhancement and arc length. Consequently, the extremely long double-helicoid [see Figs. 2(g) and 3(g)] and sextuple-helicoid [see Fig. 4(i)] surface phonon modes on the semi-infinite surfaces may facilitate catalysis if the phonon frequency is in resonance with certain midsteps in the reaction. Certainly, these are merely preliminary hypotheses. Possible applications of these topological phonons in semiconductors will necessitate additional research in the future.

Note that the nodal point phonons at the HSPs in 2D and 3D semiconductors are essential degeneracies. Hence, one can search for the semiconductors with nodal point phonons based on the SG numbers, as shown in Table S1 (see Ref. [98]). From Table S1, one can find the matrix representations of the generating elements, the species, the HSPs, and the materials candidates of the essential degeneracy. Moreover, the topological points located at the HSPs of the BZ are stable and are called symmetry-enforced band crossing points. Therefore these nodal point phonons in Table S1 (see Ref. [98]) are robust against perturbations that preserve symmetry.

Finally, we adopted 3×3×3 and 2×2×2 supercell sizes for some semiconductors with nodal point phonons on the high-symmetry lines to calculate the force constants, and then determined the phonon dispersions. The results are shown in Table S2 (see Ref. [98]), one can guarantee their phonon spectra convergence and finds that the topological phonons on the high-symmetry lines still appear in the phonon dispersions of these semiconductors.

XIV. COMPUTATIONAL METHODS

We carried out the first-principles calculations using the Vienna *ab initio* simulation package (VASP) [130,131]. The projector augmented-wave (PAW) [132] method was used for the plane-wave basis. Electronic wave functions were expanded in a plane-wave basis set with a well converged cutoff energy of 500 eV, and 7×7×7 Monkhorst-Pack k meshes for Ag_2HgI_4, 9×9×7 k meshes for $SrGeTeO_6$, 11×11×5 k meshes for HgO, 7×7×9 k meshes for Y_3CuGeS_7, 9×9×9 k meshes for SbIrS, 7×7×11 k meshes for Ge_3N_4, 9×9×5 k meshes for TeO_2, 3×3×3 k meshes for $Ge_{19}(PBr)_4$, 9×9×9 k meshes for $MgTe_2$, 9×9×9 k meshes for ZrSO, 9×9×5 k meshes for MgTe, 9×9×9 k meshes for Hf_3N_4, 5×7×4 k meshes for $RbGaH_2$, 7×7×4 k meshes for CsNaSe, 5×5×5 k meshes for CdS_2, 7×7×7 k meshes for Au_2S, 5×5×5 k meshes for Tl_2PtCl_6, 5×5×5 k meshes for K_2S, 9×9×7 k meshes for LiBeN, 9×9×5 k meshes for AgI, 5×5×7 k meshes for $YAgTe_2$, 9×9×9 k meshes for CdO_2, 9×7×1 k meshes for PbO, and 15×15×1 k meshes for $PbSe_2$ were large enough to be separately used for integration in the irreducible BZ throughout the calculations. The exchange-correlation interactions were described by the Perdew-Burke-Ernzerhof (PBE) functional within the generalized gradient approximation (GGA) [133]. During structural optimizations, the lattice constants and atomic positions were fully relaxed until the total energy and atomic force were less than 10^{-6} eV and 0.01 eV/Å, respectively. We used the density functional perturbation theory [134] to obtain the force constants, as

implemented in the VASP. Then, we used the PHONOPY package [135] to calculate the phonon dispersion spectrum. A phonon tight-binding Hamiltonian was constructed using the open-source software WANNIERTOOLS code [136]. Green's function iterative method [137,138] was used to obtain surface/edge states for these 3D/2D semiconductors. We also employed the Wilson loop method [139] to determine the Chern numbers or topological charge of WPs. The calculations of the Chern numbers of nodal points were implemented in the Wanniertools code [136]. The IRRs of the phonon spectrum are obtained by the recently released package PHONONIREP [140], which is developed based on the SPACEGROUPIREP package [141].

ACKNOWLEDGMENTS

This paper was supported by the National Key R&D Program of China (Grant No. 22022YFA1402600), the National Natural Science Foundation of China (Grants No. 51801163), and the Natural Science Foundation of Chongqing (Grant No. CSTB2022NSCQ-MSX0283).

[1] B. A. Bernevig and S.-C. Zhang, Phys. Rev. Lett. **96**, 106802 (2006).
[2] B. A. Bernevig, T. L. Hughes, and S.-C. Zhang, Science **314**, 1757 (2006).
[3] Y. Ou, C. Liu, G. Jiang, Y. Feng, D. Zhao, W. Wu, X.-X. Wang, W. Li, C. Song, L.-L. Wang, W. Wang, W. Wu, Y. Wang, K. He, X.-C. Ma, and Q.-K. Xue, Adv. Mater. **30**, 1703062 (2018).
[4] L. Pan, A. Grutter, P. Zhang, X. Che, T. Nozaki, A. Stern, M. Street, B. Zhang, B. Casas, Q. L. He *et al.*, Adv. Mater. **32**, 2001460 (2020).
[5] M. Z. Hasan and C. L. Kane, Rev. Mod. Phys. **82**, 3045 (2010).
[6] J. E. Moore, Nature (London) **464**, 194 (2010).
[7] J. Liu and T. Hesjedal, Adv. Mater. **35**, 2102427 (2023).
[8] S. Bhattacharyya, G. Akhgar, M. Gebert, J. Karel, M. T. Edmonds, and M. S. Fuhrer, Adv. Mater. **33**, 2007795 (2021).
[9] M.-H. Du, J. Yan, V. R. Cooper, and M. Eisenbach, Adv. Funct. Mater. **31**, 2006516 (2021).
[10] P. Wei, J. Yang, L. Guo, S. Wang, L. Wu, X. Xu, W. Zhao, Q. Zhang, W. Zhang, M. S. Dresselhaus, and J. Yang, Adv. Funct. Mater. **26**, 5360 (2016).
[11] H. Chorsi, B. Cheng, B. Zhao, J. Toudert, V. Asadchy, O. F. Shoron, S. Fan, and R. Matsunaga, Adv. Funct. Mater. **32**, 2110655 (2022).
[12] A. D. Rice, C. H. Lee, B. Fluegel, A. G. Norman, J. N. Nelson, C. S. Jiang, M. Steger, D. L. McGott, P. Walker, and K. Alberi, Adv. Funct. Mater. **32**, 2111470 (2022).
[13] M. Khazaei, A. Ranjbar, Y. Kang, Y. Liang, R. Khaledialidusti, S. Bae, H. Raebiger, V. Wang, M. J. Han, H. Mizoguchi, M. S. Bahramy, T. D. Kühne, R. V. Belosludov, K. Ohno, and H. Hosono, Adv. Funct. Mater. **32**, 2110930 (2022).
[14] H. H. Wang, X. G. Luo, K. L. Peng, Z. L. Sun, M. Z. Shi, D. H. Ma, N. Z. Wang, T. Wu, J. J. Ying, Z. F. Wang, and X. H. Chen, Adv. Funct. Mater. **29**, 1902437 (2019).
[15] W. Liu, Z. Wang, J. Wang, H. Bai, Z. Li, J. Sun, X. Zhou, J. Luo, W. Wang, C. Zhang, J. Wu, Y. Sun, Z. Zhu, Q. Zhang, and X. Tang, Adv. Funct. Mater. **32**, 2202143 (2022).
[16] B. Q. Lv, T. Qian, and H. Ding, Rev. Mod. Phys. **93**, 025002 (2021).
[17] J. Hu, S. Xu, N. Ni, and Z. Mao, Annu. Rev. Mater. Res. **49**, 207 (2019).
[18] H. Gao, J. W. Venderbos, Y. Kim, and A. M. Rappe, Annu. Rev. Mater. Res. **49**, 153 (2019).
[19] B. Yan, and C. Felser, Annu. Rev. Condens. Matter Phys. **8**, 337 (2017).
[20] S. Lei, S. M. L. Teicher, A. Topp, K. Cai, J. Lin, G. Cheng, T. H. Salters, F. Rodolakis, J. L. McChesney, and S. Lapidus *et al.*, Adv. Mater. **33**, 2101591 (2021).
[21] H. Xu, J. Wei, H. Zhou, J. Feng, T. Xu, H. Du, C. He, Y. Huang, J. Zhang, Y. Liu, H.-C. Wu, C. Guo, X. Wang, Y. Guang, H. Wei, Y. Peng, W. Jiang, G. Yu, and X. Han, Adv. Mater. **32**, 2000513 (2020).
[22] L. D. Anh, K. Takase, T. Chiba, Y. Kota, K. Takiguchi, and M. Tanaka, Adv. Mater. **33**, 2104645 (2021).
[23] N. P. Armitage, E. J. Mele, and A. Vishwanath, Rev. Mod. Phys. **90**, 015001 (2018).
[24] S. M. Young and C. L. Kane, Phys. Rev. Lett. **115**, 126803 (2015).
[25] Y. Shao, A. N. Rudenko, J. Hu, Z. Sun, Y. Zhu, S. Moon, A. J. Millis, S. Yuan, A. I. Lichtenstein, D. Smirnov, Z. Q. Mao, M. I. Katsnelson, and D. N. Basov, Nat. Phys. **16**, 636 (2020).
[26] T. Feng, P. S. Wang, Z. J. Han, L. Zhou, W. Q. Zhang, Q. H. Liu, and W. S. Liu, Adv. Mater. **34**, 2200931 (2022).
[27] S. Chi, F. Liang, H. Chen, W. Tian, H. Zhang, H. Yu, G. Wang, Z. Lin, J. Hu, and H. Zhang, Adv. Mater. **32**, 1904498 (2020).
[28] T.-R. Chang, I. Pletikosic, T. Kong, G. Bian, A. Huang, J. Denlinger, S. K. Kushwaha, B. Sinkovic, H.-T. Jeng, T. Valla, W. Xie, and R. J. Cava, Adv. Sci. **6**, 1800897 (2019).
[29] H. Huang, J. Liu, D. Vanderbilt, and W. Duan, Phys. Rev. B **93**, 201114(R) (2016).
[30] W. Wu, Y. Liu, S. Li, C. Zhong, Z.-M. Yu, X.-L. Sheng, Y. X. Zhao, and S. A. Yang, Phys. Rev. B **97**, 115125 (2018).
[31] S. Z. Chen, S. Li, Y. Chen, and W. Duan, Nano Lett. **20**, 5400 (2020).
[32] B. B. Fu, C. J. Yi, T. T. Zhang, M. Caputo, J. Z. Ma, and X. Gao *et al.*, Sci. Adv. **5**, eaau6459 (2019).
[33] M. Xiao, L. Ye, C. Qiu, H. He, Z. Liu, and S. Fan, Sci. Adv. **6**, eaav2360 (2020).
[34] Y. Qie, J. Liu, S. Wang, Q. Sun, and P. Jena, J. Mater. Chem. A **7**, 5733 (2019).
[35] K. Sivula and R. van de Krol, Nat. Rev. Mater. **1**, 15010 (2016)
[36] M. N. Yoder, IEEE Trans. Electron Devices **43**, 1633 (1996).
[37] Z. Wang, P. K. Nayak, J. A. Caraveo-Frescas, and H. N. Alshareef, Adv. Mater. **28**, 3831 (2016).
[38] L. I. Berger, *Semiconductor Materials* (CRC Press, London, 1996).
[39] Y. Singh, *Semiconductor Devices* (IK International Pvt Ltd, New Delhi, 2013).
[40] T. Ideue, M. Hirayama, H. Taiko, T. Takahashi, M. Murase, T. Miyake, S. Murakami, T. Sasagawa, and Y. Iwasa, Proc. Natl. Acad. Sci. USA **116**, 25530 (2019).
[41] M. Sakano, M. Hirayama, T. Takahashi, S. Akebi, M. Nakayama, K. Kuroda, K. Taguchi, T. Yoshikawa, K.

Miyamoto, T. Okuda *et al.*, Phys. Rev. Lett. **124**, 136404 (2020).
[42] B. T. Fu, D. S. Ma, C. He, Y. H. Zhao, Z. M. Yu, and Y. G. Yao, Phys. Rev. B **105**, 035126 (2022).
[43] T. Tan, X. Jiang, C. Wang, B. Yao, and H. Zhang, Adv. Sci. **7**, 2000058 (2020).
[44] L. Zhang, J. Ren, J.-S. Wang, and B. Li, Phys. Rev. Lett. **105**, 225901 (2010).
[45] Y. Liu, X. Chen, and Y. Xu, Adv. Funct. Mater. **30**, 1904784 (2020).
[46] X.-Q. Chen, J. Liu, and J. Li, Innovation **2**, 100134 (2021).
[47] J. Li, J. Liu, S. A. Baronett, M. Liu, L. Wang, R. Li, Y. Chen, D. Li, Q. Zhu, and X. Q. Chen, Nat. Commun. **12**, 1204 (2021).
[48] X. Wang, T. Yang, Z. Cheng, C. Surucu, J. Wang, F. Zhou, Z. Y. Zhang, and G. Zhang, Appl. Phys. Rev. **9**, 041304 (2022).
[49] Y. Liu, Y. Xu, and W. Duan, Natl. Sci. Rev. **5**, 314 (2018).
[50] O. Stenull, C. L. Kane, and T. C. Lubensky, Phys. Rev. Lett. **117**, 068001 (2016).
[51] R. Süsstrunk and S. D. Huber, Proc. Natl. Acad. Sci. USA **113**, E4767 (2016).
[52] E. Prodan and C. Prodan, Phys. Rev. Lett. **103**, 248101 (2009).
[53] O. Stenull and T. C. Lubensky, Phys. Rev. Lett. **122**, 248002 (2019).
[54] G. Ding, C. Xie, J. Bai, Z. Cheng, X. Wang, and W. Wu, Phys. Rev. B **108**, L020302 (2023).
[55] Y. Yang, C. Xie, Y. Cui, X. Wang, and W. Wu, Phys. Rev. B **107**, 054310 (2023).
[56] S. Singh, Q. S. Wu, C. Yue, A. H. Romero, and A. A. Soluyanov, Phys. Rev. Mater. **2**, 114204 (2018).
[57] B. Peng, Y. Hu, S. Murakami, T. Zhang, and B. Monserrat, Sci. Adv. **6**, eabd1618 (2020).
[58] B. Peng, A. Bouhon, B. Monserrat, and R.-J. Slager, Nat. Commun. **13**, 423 (2022).
[59] B. Peng, S. Murakami, B. Monserrat, and T. Zhang, npj Comput. Mater. **7**, 195 (2021).
[60] T. T. Zhang, H. Miao, Q. Wang, J. Q. Lin, Y. Cao, G. Fabbris, A. H. Said, X. Liu, H. C. Lei, Z. Fang, H. M. Weng, and M. P. M. Dean, Phys. Rev. Lett. **123**, 245302 (2019).
[61] B. W. Xia, R. Wang, Z. J. Chen, Y. J. Zhao, and H. Xu, Phys. Rev. Lett. **123**, 065501 (2019).
[62] T. A. Hameed, I. M. E. Radaf, and G. B. Sakr, Appl. Phys. A **124**, 684 (2018).
[63] A. A. Soluyanov, D. Gresch, Z. Wang, Q. Wu, M. Troyer, X. Dai, and B. A. Bernevig, Nature (London) **527**, 495 (2015).
[64] R. Li, B. Lv, H. Tao, J. Shi, Y. Chong, B. Zhang, and H. Chen, Natl. Sci. Rev. **8**, nwaa192 (2021).
[65] S. Borisenko, D. Evtushinsky, Q. Gibson, A. Yaresko, K. Koepernik, T. Kim, M. Ali, J. van den Brink, M. Hoesch, A. Fedorov, E. Haubold, Y. Kushnirenko, I. Soldatov, R. Schafer, and R. J. Cava, Nat. Commun. **10**, 3424 (2019).
[66] C. Fang, L. Lu, and L. Fu, Nat. Phys. **12**, 936 (2016).
[67] C. Fang, M. J. Gilbert, X. Dai, and B. A. Bernevig, Phys. Rev. Lett. **108**, 266802 (2012).
[68] T. T. Zhang, R. Takahashi, C. Fang, and S. Murakami, Phys. Rev. B **102**, 125148 (2020).
[69] Q. Chen, F. Chen, Y. Pan, C. Cui, Q. Yan, L. Zhang, Z. Gao, S. A. Yang, Z.-M. Yu, and H. Chen *et al.*, Nat. Commun. **13**, 7359 (2022).
[70] Z.-M. Yu, Z. Zhang, G.-B. Liu, W. Wu, X.-P. Li, R.-W. Zhang, S. A. Yang, and Y. Yao, Sci. Bull. **67**, 375 (2022).
[71] X. Wang, F. Zhou, Z. Zhang, W. Wu, Z.-M. Yu, and S. A. Yang, Phys. Rev. B **106**, 195129 (2022).
[72] I. Belopolski, P. Yu, D. S. Sanchez, Y. Ishida, T.-R. Chang, S. S. Zhang, S.-Y. Xu, H. Zheng, G. Chang, and G. Bian *et al.*, Nat. Commun. **8**, 942 (2017).
[73] S. Nie, T. Hashimoto, and F. B. Prinz, Phys. Rev. Lett. **128**, 176401 (2022).
[74] P. M. Woodward, A. W. Sleight, L.-Sh. Du, and C. P. Grey, J. Solid State Chem. **147**, 99 (1999).
[75] H. B. Nielsen and M. Ninomiya, Nucl. Phys. B **185**, 20 (1981).
[76] H. B. Nielsen and M. Ninomiya, Nucl. Phys. B **193**, 173 (1981).
[77] R. Wang, B. W. Xia, Z. J. Chen, B. B. Zheng, Y. J. Zhao, and H. Xu, Phys. Rev. Lett. **124**, 105303 (2020).
[78] Z. Huang, Z. Chen, B. Zheng, and H. Xu, npj Comput. Mater. **6**, 87 (2020).
[79] K. L. Aurivillius and I. Carlson, Acta Chem. Scand. **12**, 1297 (1958).
[80] X.-P. Li, K. Deng, B. Fu, Y. K. Li, D. S. Ma, J. F. Han, J. Zhou, S. Zhou, and Y. Yao, Phys. Rev. B **103**, L081402 (2021).
[81] G. Q. Ding, J. H. Wang, Z. M. Yu, Z. Y. Zhang, and W. H. Wang, and X. T. Wang, Phys. Rev. Mater. **7**, 014202 (2023).
[82] W. Meng, X. Zhang, Y. Liu, X. Dai, G. Liu, Y. Gu, E. Kenny, and L. Kou, Adv. Sci. **10**, 2205940 (2023).
[83] J. J. Zhu, W. K. Wu, J. Z. Zhao, H. Chen, L. F. Zhang, and S. S. A. Yang, npj Quantum Mater. **7**, 52 (2022).
[84] L. D. Gulay, O. S. Lychmanyuk, J. S. Damm, A. Pietraszko, and I. D. Olekseyuk, J. Alloys Compd. **414**, 113 (2006).
[85] H. Chen, J. Gao, L. Chen, G. Wang, H. Li, Y. Wang, J. Liu, J. Wang, D. Geng, Q. Zhang, J. Sheng, F. Ye, T. Qian, L. Chen, H. Weng, J. Ma, and X. Chen, Adv. Mater. **34**, 2110664 (2022).
[86] Z. Wang, A. Alexandradinata, R. J. Cava, and B. A. Bernevig, Nature (London) **532**, 189 (2016).
[87] J. Ma, C. Yi, B. Lv, Z. Wang, S. Nie, L. Wang, L. Kong, Y. Huang, P. Richard, and P. Zhang *et al.*, Sci. Adv. **3**, e1602415 (2017).
[88] P. Huang, X. B. Chen, P. Zhang, H. Y. Sun, S. G. Xu, W. Xiong, R. Wang, H. Zhang, Q. H. Liu, and X. W. Zhang, NPG Asia Mater. **13**, 49 (2021).
[89] J.-Z. Ma, Q.-S. Wu, M. Song, S.-N. Zhang, E. B. Guedes, S. A. Ekahana, M. Krivenkov, M. Y. Yao, S.-Y. Gao, W.-H. Fan, T. Qian, H. Ding, N. C. Plumb, M. Radovic, J. H. Dil, Y.-M. Xiong, K. Manna, C. Felser, O. V Yazyev, and M. Shi, Nat. Commun. **12**, 3994 (2021).
[90] P. Bayliss, Am. Mineral. **74**, 1168 (1989).
[91] Z.-M. Yu, W. Wu, X.-L. Sheng, Y. X. Zhao, and S. A. Yang, Phys. Rev. B **99**, 121106(R) (2019).
[92] Z. J. Chen, R. Wang, B. W. Xia, B. B. Zheng, Y. J. Jin, Y. J. Zhao, and H. Xu, Phys. Rev. Lett. **126**, 185301 (2021).
[93] Y. Feng, C. Xie, H. Chen, Y. Liu, and X. Wang, Phys. Rev. B **106**, 134307 (2022).
[94] T. Zhang, Z. Song, A. Alexandradinata, H. Weng, C. Fang, L. Lu, and Z. Fang, Phys. Rev. Lett. **120**, 016401 (2018).
[95] H. Miao, T. T. Zhang, L. Wang, D. Meyers, A. H. Said, Y. L. Wang, Y. G. Shi, H. M. Weng, Z. Fang, and M. P. M. Dean, Phys. Rev. Lett. **121**, 035302 (2018).
[96] E. Soignard, P. McMillan, C. Hejny, and K. Leinenweber, J. Solid State Chem. **177**, 299 (2004).

[97] T. G. Worlton and R. A. Beyerlein, Phys. Rev. B **12**, 1899 (1975).

[98] See Supplemental Material at http://link.aps.org/supplemental/10.1103/PhysRevB.108.075201 for the phonon LDOSs and frequency slices for TeO_2 and ZrSO, the shapes of the nodal lines in the [011] mirror plane for Tl_2PtCl_6, the shapes of nodal lines in the $k_z = 0$ and $k_z = \pi$ planes for K_2S, the matrix representations of the generating elements, the species, the HSPs, and the materials candidates of the essential degeneracy, and phonon dispersions for semiconductors with with nodal point phonons on the high-symmetry lines, etc.

[99] H. Menke and H. G. von Schnering, Z. Anorg. Allg. Chem. **395**, 223 (1973).

[100] S. Yanagisawa, M. Tashiro, and S. Anzai, J. Inorg. Nucl. Chem. **31**, 943 (1969).

[101] J. D. McCullough, L. Brewer, and L. A. Bromley, Acta Cryst. **1**, 287 (1948).

[102] W. Klemm and K. Wahl, Z. Anorg. Allg. Chem. **266**, 289 (1951).

[103] A. Zerr, G. Miehe, and R. Riedel, Nat. Mater. **2**, 185 (2003).

[104] L. Jin, Y. Liu, W. W. Yu, X. M. Zhang, G. D. Liu, and X. F. Dai, Phys. Rev. B **105**, 245141 (2022).

[105] N. Kumar, M. Yao, J. Nayak, M. G. Vergniory, J. Bannies, Z. Wang, N. B. M. Schröter, V. N. Strocov, L. Möchler, W. Shi, E. D. L. Rienks, J. L. Maões, C. Shekhar, S. S. P. Parkin, J. Fink, G. H. Fecher, Y. Sun, B. A. Bernevig, and C. Felser, Adv. Mater. **32**, 1906046 (2020).

[106] H. Fahlquist, D. Noreus, S. Callear, W. I. F. David, and B. C. Hauback, J. Am. Chem. Soc. **133**, 14574 (2011).

[107] H. Sabrowsky, E. Feldbaum-Möller, V. Winter, and P. Vogt, Z. Naturforsch. B **48**, 1837 (1993).

[108] T. A. Bither, R. J. Bouchard, W. H. Cloud, P. C. Donohue, and W. J. Siemons, Inorg. Chem. **7**, 2208 (1968).

[109] Q. B. Liu, Z. Q. Wang, and H. H. Fu, Mater. Today Phys. **24**, 100694 (2022).

[110] Q.-B. Liu, H.-H. Fu, and R. Q. Wu, Phys. Rev. B **104**, 045409 (2021).

[111] J. Wang, H. Yuan, Z.-M. Yu, Z. Zhang, and X. Wang, Phys. Rev. Mater. **5**, 124203 (2021).

[112] K. Ishikawa, T. Isonaga, S. Wakita, and Y. Suzuki, Solid State Ionics **79**, 60 (1995).

[113] G. Engel, Z. Kristallogr.-Cryst. Mater. **90**, 341 (1935).

[114] F. Zhou, H. Chen, Z.-M. Yu, Z. Zhang, and X. Wang, Phys. Rev. B **104**, 214310 (2021).

[115] X.-L. Sheng, Z.-M. Yu, R. Yu, H. Weng, and S. A. Yang, J. Phys. Chem. Lett. **8**, 3506 (2017).

[116] C. D. West, Z. Kristallogr. **88**, 97 (1934).

[117] M. Somer, W. Carrillo-Cabrera, E.-M. Peters, K. Peters, and H. G. von Schnering, Z. Kristallogr. **211**, 635 (1996).

[118] M. Wang, Y. Wang, Z. Yang, J. Fan, B. Zheng, R. Wang, and X. Wu, Phys. Rev. B **105**, 174309 (2022).

[119] Y. Yang, J. Wang, Y. Liu, Y. Cui, G. Ding, and X. Wang, Phys. Rev. B **107**, 024304 (2023).

[120] R. J. Cava, F. Reidinger, and B. J. Wuensch, Solid State Commun. **24**, 411 (1977).

[121] L. D. Gulay, I. D. Olekseyuk, and A. Pietraszko, J. Alloys Compd. **424**, 159 (2006).

[122] C. W. W. Hoffman, R. C. Ropp, and R. W. Mooney, J. Am. Chem. Soc. **81**, 3830 (1959).

[123] J. Gong, J. Wang, H. Yuan, Z. Zhang, W. Wang, and X. Wang, Phys. Rev. B **106**, 214317 (2022).

[124] Y. Jin, R. Wang, and H. Xu, Nano Lett. **18**, 7755 (2018).

[125] J. Li, L. Wang, J. Liu, R. Li, Z. Zhang, and X.-Q. Chen, Phys. Rev. B **101**, 081403(R) (2020).

[126] Y. Wang, L. Li, W. Yao, S. Song, J. Sun, J. Pan, X. Ren, C. Li, E. Okunishi, Y.-Q. Wang *et al.*, Nano Lett. **15**, 4013 (2015).

[127] W.-W. Yu, Y. Liu, W. Meng, H. Liu, J. Gao, X. Zhang, and G. Liu, Phys. Rev. B **105**, 035429 (2022).

[128] A. Ingle, M. Singh, S. Tawfik, B. Murdoch, E. Mayes, M. Spencer, R. Ramanathan, and V. Bansal, ACS Nano **16**, 10679 (2022).

[129] T. Vasileiadis, J. Varghese, V. Babacic, J. Gomis-Bresco, D. Navarro Urrios, and B. Graczykowski, J. Appl. Phys. **129**, 160901 (2021).

[130] G. Kresse and J. Hafner, Phys. Rev. B **49**, 14251 (1994).

[131] G. Kresse and J. Furthmüller, Phys. Rev. B **54**, 11169 (1996).

[132] P. E. Blöchl, Phys. Rev. B **50**, 17953 (1994).

[133] J. P. Perdew, K. Burke, and M. Ernzerhof, Phys. Rev. Lett. **77**, 3865 (1996).

[134] X. Gonze and C. Lee, Phys. Rev. B **55**, 10355 (1997).

[135] A. Togo and I. Tanaka, Scr. Mater. **108**, 1 (2015).

[136] Q.-S. Wu, S.-N. Zhang, H.-F. Song, M. Troyer, and A. A. Soluyanov, Comput. Phys. Commun. **224**, 405 (2018).

[137] M. L. Sancho, J. L. Sancho, and J. Rubio, J. Phys. F **14**, 1205 (1984).

[138] M. P. L. Sancho, J. M. L. Sancho, and J. Rubio, J. Phys. F **15**, 851 (1985).

[139] A. A. Soluyanov and D. Vanderbilt, Phys. Rev. B **83**, 235401 (2011).

[140] Z. Zhang, Z. Yu, G. Liu, and Y. Yao, arXiv:2201.11350.

[141] G. B. Liu, M. Chu, Z. Zhang, Z. M. Yu, and Y. Yao, Comput. Phys. Commun. **265**, 107993 (2021).